The physics of the mean and oscillating radial electric field in the L H transition: the driving nature and turbulent transport suppression mechanism

SPECIAL TOPIC • OPEN ACCESS

The physics of the mean and oscillating radial electric field in the L–H transition: the driving nature and turbulent transport suppression mechanism

To cite this article: T. Kobayashi 2020 *Nucl. Fusion* **60** 095001

OPEN ACCESS
IOP Publishing | International Atomic Energy Agency Nuclear Fusion
Nucl. Fusion **60** (2020) 095001 (19pp) https://doi.org/10.1088/1741-4326/ab7a67

Special Topic

The physics of the mean and oscillating radial electric field in the L–H transition: the driving nature and turbulent transport suppression mechanism

T. Kobayashi[1,2,3]

[1] National Institute for Fusion Science, National Institutes of Natural Sciences, Toki, 509-5292, Japan
[2] The Graduate University for Advanced Studies, SOKENDAI, Toki, 509-5292, Japan

E-mail: kobayashi.tatsuya@nifs.ac.jp

Received 4 January 2020, revised 14 February 2020
Accepted for publication 26 February 2020
Published 22 July 2020

Abstract

The low-to-high confinement mode transition (L–H transition) is one of the key elements in achieving a self-sustained burning fusion reaction. Although there is no doubt that the mean and/or oscillating radial electric field plays a role in triggering and sustaining the edge transport barrier, the detailed underlying physics are yet to be unveiled. In this special topic paper, the remarkable progress achieved in recent years is reviewed for two different aspects: (i) the radial electric field driving procedure and (ii) the turbulent transport suppression mechanism. Experimental observations in different devices show possible conflicting natures for these phenomena, which cannot be resolved solely by conventional paradigms. New insights obtained by combining different model concepts successfully reconcile these conflicts.

Keywords: L-H transition, radial electric field, radial current, turbulent transport, cross phase, turbulence trapping

(Some figures may appear in colour only in the online journal)

1. Introduction

Magnetically confined plasmas, typified by tokamaks and stellarators, are non-equilibrium open systems, in which inherent sources and sinks of particles, momentum, and heat exist in the system. One of the ultimate industrial applications of high temperature magnetically confined plasmas is thermonuclear fusion energy development. To realize a sustainable nuclear reaction in a fusion plant, one has to achieve a sufficiently high plasma performance with a tolerable heat exhaust for the plasma-facing components. Increasing the heat input with the aim to raise the plasma temperature leads to confinement degradation [1] which is considered to be brought about by plasma turbulence, resulting in unacceptable heat flow to the material divertor. Meanwhile, a spontaneous transition to the suppressed turbulence state with improved plasma confinement occurs by applying intense heating power above a threshold value [2]. Plasmas before and after this confinement transition are called the L-mode state and the H-mode state, respectively, and have different physical properties. The H-mode plasma is the prototypical example of the dissipative structure spontaneously formed in the open system [3] and has an attractive nature suitable for use in controlled

[3] This special topic paper is dedicated to the memory of Professor Sanae-I. Itoh (2019 *Plasma Phys. Control. Fusion* **62** 020101).

thermonuclear fusion reactors [4]. Therefore, unveiling the background physics of the L–H mode transition is desirable from both the academic and industrial points of view.

Since the first discovery of the L–H transition [5], the underlying physics of the transition have been investigated intensively. The important role of the radial electric field bifurcation for the L–H transition has been pointed out theoretically [6, 7], and the existence of the negative radial electric field structure localized at the plasma periphery was spectroscopically measured in the H-mode [8, 9]. Further understanding of confinement improvement was achieved through turbulence measurement. Across the L–H transition, the turbulence fluctuation amplitude was found to be reduced, which is considered to be responsible for the suppression of turbulent transport [10–15]. A sheared radial electric field or sheared $E \times B$ flow [16] was regarded as the major factor for turbulence amplitude suppression, which stretches turbulence eddies out causing thermalization or turns the turbulence into the large scale mean flow [17–19]. This prevailing concept is referred to as the shear-amplitude paradigm in this paper.

Despite the continuous effort that has steadily advanced our understanding of the background physics of the L–H transition, some open questions still remain [20]. In this paper, two of these questions are focused upon. The first open question is how the radial electric field is driven. Several theoretical concepts for the radial electric field driving mechanism at the edge region have been proposed, and experimental validation for these models has been an active research topic. Nevertheless, a comprehensive model that can cover a wide range of observations has not yet been acquired, although some plausible case studies for validation of various model concepts have been reported in different plasma regimes or experimental devices. The second open question is how the turbulent transport is quenched by the non-uniform radial electric field structure. This transport suppression occurs in a wide radial range of the plasma, not only in the sheared radial electric field region but also in the shear-less part, i.e. at the bottom of the E_r-well structure or the core region. Recent observations have shown that some ingredients beyond the shear-amplitude suppression paradigm are necessary to capture the whole picture of the transport suppression across the transition.

In this paper, we review recent experimental observations and theoretical and numerical works to examine the two open questions raised above, aiming towards establishing a comprehensive model of the L–H transition. Accordingly, sections 2 and 3 are dedicated to topics regarding the radial electric field drive and the turbulent transport suppression, respectively. The last subsections in sections 2 and 3 discuss the issues remaining for future study. A summary of the paper is provided in section 4.

2. Radial electric field driving mechanism

Naturally, plasma is regarded as quasi-neutral. But in reality, there are several mechanisms through which a toroidal plasma can form the radial electric field structure by itself [21]. First, classical concepts for the possible candidates for the radial electric field excitation are presented in this section, and then key experimental implications that provide a perspective for model validation are introduced. Considering these bases, cutting-edge results of experimental observations and numerical simulations are reviewed. Finallly, an open issue for quantitative model validation, i.e. the relative dielectric constant in toroidal plasmas involving inertia enhancement, is discussed.

2.1. Classical concepts of radial electric field driving in toroidal plasmas

In this paper, two major categories of the radial electric field driving mechanism are discussed. The first category is the radial electric field excitation due to different trajectories of ions and electrons that induce radial charge separation. The neoclassical bulk viscosity [7, 22] is one of the representative concepts in this category. The neoclassical bulk viscosity is predicted to induce excess ion current in the radial direction

$$J_{\mathrm{i}}^{\mathrm{BV}} = -enD_{\mathrm{p}}\left[\frac{n'}{n} + \gamma_j \frac{T'}{T} - \frac{e}{T}(E_r - B_\theta V_{||})\right]\exp(-X^2), \quad (1)$$

where $\gamma_j = 3/2$ in the plateau regime, the prime denotes the radial derivative, and $D_{\mathrm{p}} = (\pi/2)(\epsilon_{\mathrm{t}} q \rho_{\mathrm{i}} T/reB)$ is the characteristic diffusivity. Other quantities are as follows: e is the electron charge, n is the plasma density, T is the plasma temperature, B_θ is the poloidal magnetic field, $V_{||}$ is the parallel velocity, ϵ_{t} is the inverse aspect ratio, q is the safety factor, $\rho_{\mathrm{i}} = \sqrt{mT}/eB$ is the ion gyro-radius, and $\rho_{\mathrm{p}} = q\epsilon_{\mathrm{t}}^{-1}\rho_{\mathrm{i}}$ is the ion poloidal gyro-radius. This ion current initiates the radial electric field excitation, and when the excited radial electric field balances with the gradient terms and the parallel velocity term, the ion current disappears. The normalized radial electric field X is defined as

$$X \equiv \rho_{\mathrm{p}} eE_r/T. \quad (2)$$

The exponential function $\exp(-X^2)$ rapidly goes to zero once the normalized radial electric field exceeds unity.

Only at the edge can the ion particles escape from the confinement magnetic field due to its larger radial excursion, which excites the negative radial electric field [6, 7]. The magnitude of this ion orbit loss current is predicted to be

$$J_{\mathrm{i}}^{\mathrm{LC}} = en\nu_{\mathrm{ii}}\rho_{\mathrm{p}}\exp(-X^2), \quad (3)$$

where ν_{ii} is the ion–ion collision frequency. The outward ion current is reduced when the normalized radial electric field exceeds unity. The above two currents are functions of the kinetic profile and its gradient, therefore these radial currents can vary in the profile time scale.

The second category of the radial electric field excitation is that related to the turbulence dynamics. The well known fluid Reynolds stress for the poloidal flow drive can be categorized here. The zonal flow is excited by the fluid Reynolds stress via the modulational instability process [23–27], which is considered to play an important role in the predator–prey dynamics [28], as will be discussed in detail below. In magnetized plasmas, the radial electric field and the poloidal flow

are related through the $E \times B$ motion. The equivalent radial current can be quantified as

$$J_{\mathrm{i}}^{\mathrm{v}\nabla\mathrm{v}} = -en\omega_{\mathrm{ci}}^{-1} r^{-1} \frac{\partial r \Pi_{r\theta}}{\partial r}, \quad (4)$$

where ω_{ci} is the ion-gyro angular frequency [29].

Another possibility is the wave convection of momentum. This produces excess electron flux at the edge, while in the core this is compensated by ions. The intuitive expression of this radial current is given as

$$J_{\mathrm{e-i}}^{\mathrm{WC}} = -enD_{\mathrm{e}}\rho_{\mathrm{p}}^{-1}(-\lambda - X), \quad (5)$$

where $\lambda = -\rho_{\mathrm{p}} n^{-1} n'$ is the normalized inverse density gradient length and D_{e} is the typical turbulent diffusivity [6]. The radial currents related to turbulence dynamics can change quickly with the turbulence time scale, which is one of the major differences from the radial currents in the first category.

The charge separation due to these radial currents induce the radial electric field of

$$-\epsilon_{\perp}\epsilon_0 \frac{\partial E_r}{\partial t} = J_{\mathrm{i}}^{\mathrm{BV}} + J_{\mathrm{i}}^{\mathrm{LC}} + J_{\mathrm{i}}^{\mathrm{v}\nabla\mathrm{v}} - J_{\mathrm{e-i}}^{\mathrm{WC}} - J_{\mathrm{i}}^{\mathrm{CX}} + J^{\mathrm{other}}, \quad (6)$$

where $J_{\mathrm{i}}{}^{\mathrm{CX}}$ is the charge exchange current damping term and $\epsilon_{\perp}$ is the relative dielectric constant of the plasma [21]. For quantitative model validation, what model is used as the relative dielectric constant in toroidal plasmas is essential [30–33], which will be discussed below. Imbalance among the current terms in equation (6) in the L-mode induces radial electric field growth, which breaks the steady state condition and pushes the plasma into the H-mode.

The radial currents induced by other possible mechanisms and external operations, J^{other}, are also worth considering. For example, the MHD mode involving magnetic island activities can create an enhanced electron loss channel by short-circuiting the nested magnetic surfaces [34, 35]. As a result of this electron loss, the negative radial electric field structure in the H-mode is weakened and concomitant confinement degradation occurs. Another important factor for the current balance equation is the radial current induced by external biassing [36–40]. In these cases, the finite radial current applied externally is balanced by other terms in equation (6) in the stationary state, as predicted in [41]. The $E \times B$ flow is accelerated by the $J_r \times B$ force of the bulk radial plasma current that flows in the opposite direction to the externally applied current to satisfy the balanced current condition.

2.2. Possible bifurcation in toroidal plasmas

As discussed above, the ambipolar particle fluxes, i.e. the radial currents, are nonlinear functions of the radial electric field. By balancing them in the steady state condition of $\partial E_r/\partial t = 0$, the bifurcation conditions of the radial electric field were explored. For example, Itoh and Itoh found an E_r bifurcation by balancing the ion orbit loss flux and the wave convection flux [6]. In this case, more than two intersections of the ion orbit loss flux curve and the wave convection flux curve at different E_r values were pointed out as possible steady state conditions. Meanwhile, Shaing and Crume Jr found another type of bifurcation by comparing the ion orbit loss flux and the neoclassical bulk viscosity flux [7].

A different way to reach the H-mode, the so-called predator–prey model, was proposed by Kim and Diamond [28]. This model is not based on the condition $\partial E_r/\partial t = 0$, but adopts a dynamic interplay among turbulence, zonal flow, and mean flow. As a result of the interplay, a consecutive sequence of L–H transitions and H–L back-transitions, the so-called limit cycle oscillation, occurs between the turbulence and zonal flow, which gradually steepens the edge pressure gradient. Once the pressure gradient driven mean flow reaches a threshold value, the turbulence and the zonal flow are totally quenched and the H-mode transition occurs.

Another type of bifurcation mechanism based on the transport flux equation nonlinearly depending on the radial electric field shear was proposed by Staebler and co-workers[42]. A set of system equations is closed by assuming that the radial electric field is generated by gradients, and a bifurcation is reproduced by choosing a specific range of coefficients.

2.3. Key experimental observations

In order to achieve a comprehensive understanding of the radial electric field excitation mechanisms, numerous experiments have been performed. In this subsection, some of the key experimental observations that are useful for validating theoretical models are introduced.

First, let us consider the time scale of the radial electric field excitation, in which an important role of turbulence at the transition is implied. Figure 1 shows the radial profiles of the radial electric field and the pressure gradient before and immediately after the transition measured by electrostatic probes in DIII-D [43]. Although the radial electric field profile shows a significant change before and after the transition, the pressure gradient profile remains almost identical. Figure 2 shows the relation between the $E \times B$ shearing rate $\omega_{E\times B} = (r/q)\mathrm{d}[(q/r)(E/B)]/\mathrm{d}r$ and the ion temperature gradient across the L–H transition in JT-60U [44]. Around $t \sim 5.1$ s, where forward and back transitions occur, the value of $\omega_{E\times B}$ jumps without being accompanied by any change in the ion temperature gradient. These two observations clearly show that the radial electric field can change before the density profile or the temperature profile change. The L–H transition can occur in a very short time scale in $O(10\ \mu\mathrm{s})$ to $O(100\ \mu\mathrm{s})$ [15]. This time scale is clearly the turbulence time scale, and seems not to be the profile time scale. The density profile and the temperature profile start to form a pedestal structure after the excited radial electric field suppresses the turbulent transport.

Once the transition is initiated, the radial electric field profile continues to develop until it subsides with some saturation mechanisms. Next, we discuss where the radial electric field finally settles in the H-mode. Figure 3(a) shows the radial profile of the radial electric field in the H-mode in ASDEX-Upgrade [45]. The radial profile of the radial electric field is evaluated using charge exchange recombination spectroscopy

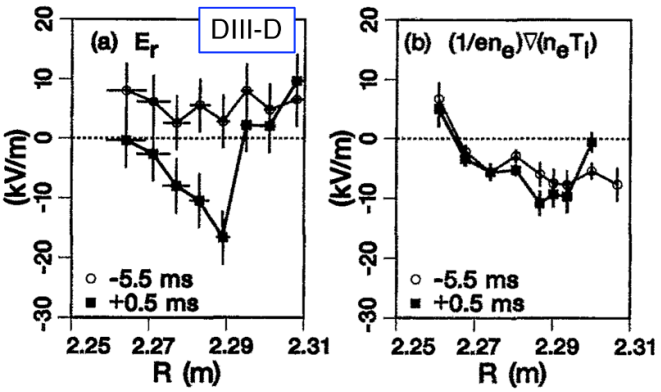

Figure 1. Radial profiles of (*a*) the radial electric field and (*b*) the pressure gradient before and immediately after the transition. Reprinted from [43], with the permission of AIP Publishing.

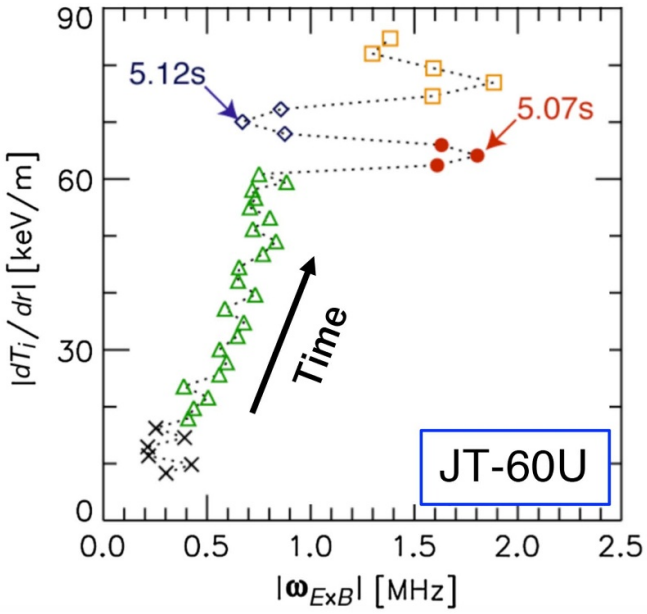

Figure 2. Relation between the $E \times B$ shearing rate and the ion temperature gradient across the L–H transition. Reprinted figure with permission from [44], Copyright 2010 by the American Physical Society.

through the radial force balance equation

$$E_r = \frac{\nabla p_j}{Z_j e n_j} - V_{\theta,j} B_\phi + V_{\phi,j} B_\theta, \tag{7}$$

where the subscript j denotes the ion species of interest, p is the ion pressure, Z is the ion charge, V_θ and V_ϕ are the ion poloidal and toroidal rotation velocities, and B_θ and B_ϕ are the poloidal and toroidal magnetic fields, respectively. In addition, the radial electric field profiles predicted by a theoretical model [46] and by a numerical code [47], and the pressure gradient term in equation (7) are shown. It is proven that the neoclassical theory can account for the main features of the radial electric field structure.

Also in ASDEX-Upgrade, it was shown that the radial electric field value settles at a specific threshold value determined by neoclassical theory at the transition in a wide range of plasma parameters (figure 3(*b*)) [48]. This observation indicates the crucial role of neoclassical theory in maintaining the radial electric field structure in the H-mode. It is generally accepted that the threshold power of the L–H transition strongly depends on the plasma density, and has a minimum value at the specific range of the density [49, 50]. Nevertheless, the threshold neoclassical radial electric field shows no plasma density dependence, providing a unique physical criterion for the L–H transition condition. The input power that is necessary for exciting the threshold neoclassical radial electric field is therefore considered to strongly depend on the plasma density, and probably suggests different paths to achieve the threshold value below and above the density minimum. Moreover, turbulence is often totally quenched and the transport level decays down to the neoclassical level in the H-mode [51] so that the turbulence originating part of the radial electric field cannot remain essential.

There are two contradictory aspects at a first glance, i.e. the important role of the turbulence in accounting for the fast time scale of the transition and the converging feature of the radial electric field to the neoclassical value in the steady state H-mode. These can be reconciled by considering possible combinations of multiple driving mechanisms that may reproduce the complex transition sequence. Hereafter, model validation methods taking into account different combinations of multiple concepts will be introduced from recent experimental and numerical works.

2.4. Recent model validation efforts

The first case is from the JFT-2M data analysis study [29, 52, 53]. The electrostatic potential and the electron density at four radial locations were simultaneously measured with a heavy ion beam probe (HIBP) [54, 55]. From the obtained dataset, equation (6) was directly examined, as was first performed in the heliotron CHS [56]. Figure 4 shows the relation between the normalized radial electric field and the radial current across the L–H transition [29]. The black curve is the trajectory of the experimental observation and the red curve is the E_r driven by the neoclassical current (equation (1)) and the ion orbit loss current (equation (3)). The experimental value of the radial current is estimated by $J_r = -\epsilon_\perp \epsilon_0 \partial E_r/\partial t$, where E_r is evaluated as the radial difference of the electrostatic potential directly measured by the HIBP. The confinement states of the plasma are indicated by the labels at the top of the figure. The transition sequence seen in the experimental trajectory is as follows: when the plasma is in the L-mode, the normalized radial electric field $X = \rho_p e E_r/T$ is close to zero and the radial current oscillates around zero. At the transition, the positive radial current is excited, leading to charge separation, which deepens the negative radial electric field. The positive radial current peaks at $3-4$ A/m^2, and decreases towards zero. At $X \sim 1$ and $J_r \sim 0$, the plasma is considered to be in the H-mode. A few milliseconds later, another transition occurs that

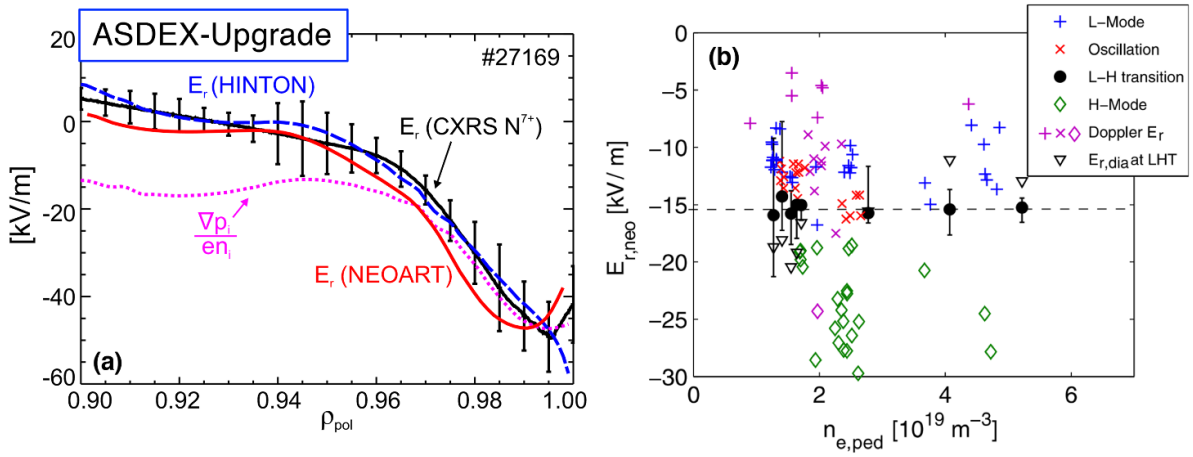

Figure 3. (*a*) Radial profile of the radial electric field profiles, experimentally measured and theoretically predicted. (*b*) Density dependence of the threshold neoclassical radial electric field. Reproduced courtesy of IAEA. Figure from [48]. Copyright 2011 IAEA.

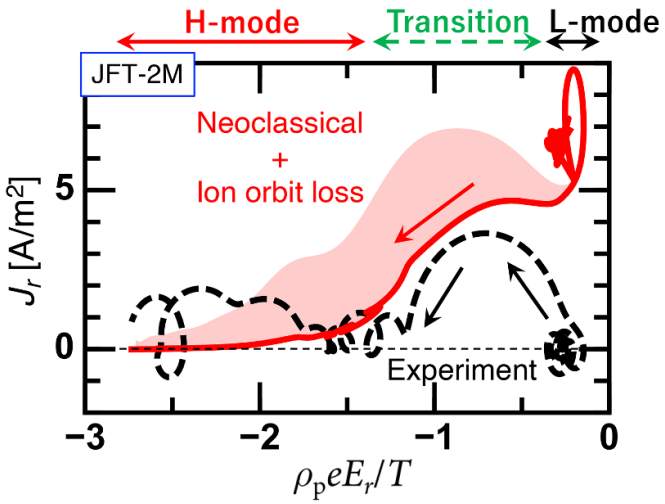

Figure 4. Relation between the normalized radial electric field and the radial current across the L–H transition. Reproduced from [29]. CC BY 4.0.

further enhances the negative radial electric field, but it is beyond the focus of this paper. At the first transition, the sum of the neoclassical bulk viscosity and the ion orbit loss approximately accounts for the experimental value. However, there is a significant mismatch in the L-mode, where the theoretical models overestimate the radial current of $\sim$5 A/m^2. If one admits that the model expressions of equations (1) and (3) are valid, there must be a negative radial current component that compensates the excess positive radial current. The radial current that is equivalent to the fluid Reynolds stress force (equation (4)) is directly estimated by the turbulence measurement and it is found to play a minor role in the L-mode. As another candidate, the wave convection process (equation (5)) is examined and found to possibly account for the L-mode current balance.

A scenario of the radial electric field excitation at the L–H transition is deduced as follows. In the L-mode, the radial current balance is satisfied by three components, by the neoclassical bulk viscosity current $J_{\rm i}{}^{\rm BV}$, the ion orbit loss current $J_{\rm i}{}^{\rm LC}$, and the wave convection current $J_{\rm e-i}{}^{\rm WC}$, i.e.

$$-\epsilon_\perp\epsilon_0\frac{\partial E_r}{\partial t} = J_{\rm i}^{\rm BV} + J_{\rm i}^{\rm LC} - J_{\rm e-i}^{\rm WC} = 0. \tag{8}$$

As described in [6], the magnitude of the turbulence diffusivity in equation (5) is sensitive to the radial electric field. Once the radial electric field grows above a certain value, $J_{\rm e-i}{}^{\rm WC}$ is suppressed and the current imbalance is enhanced, which facilitates further growth of the radial electric field, i.e.

$$-\epsilon_\perp\epsilon_0\frac{\partial E_r}{\partial t} = J_{\rm i}^{\rm BV} + J_{\rm i}^{\rm LC} - \cancel{J_{\rm e-i}^{\rm WC}} \neq 0. \tag{9}$$

The excited radial currents through the neoclassical process and the ion orbit loss process are suppressed when the normalized radial electric field X approaches unity.

When the applied heating power is marginal with respect to the threshold power for transition, the limit cycle oscillation (LCO), is frequently observed in many toroidal plasmas [57–70]. The LCO phase provides a chance to investigate the basic mechanism of the radial electric field excitation thanks to its repetitive nature, which offers multiple independent events for statistical approaches. Some of them are considered to be consistent with the predator–prey model [28], in which the combination between the turbulence contribution and the profile contribution for the radial electric field drive plays a role. Figure 5 shows the time evolution of the L–H transition involving the LCO in DIII-D [60]. Once the LCO is triggered, an oscillation with nearly constant frequency is observed in the D_α emission signal, which is regarded as repetitive transport barrier formation and deformation. Panels (*a*) and (*b*) in figure 5 show the $E\times B$ velocity shearing rate $\omega_{E\times B}$ and its pressure gradient driven part $\omega_{E\times B\ {\rm dia}}$. The LCO is driven by the radial electric field shear oscillation. In the beginning, the radial electric field shear oscillation is considered to be turbulence driven zonal flow. Only a minor contribution of the pressure gradient driven part to the LCO is seen. However, in the later phase

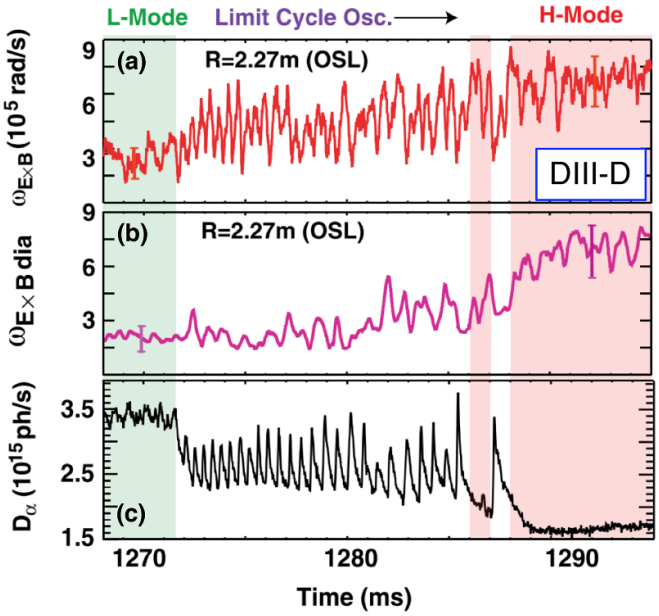

Figure 5. Time evolutions of (*a*) the $E \times B$ shearing rate, (*b*) the diamagnetic part of the $E \times B$ shearing rate, and (*c*) the D_α emission intensity. Reprinted figure with permission from [60], Copyright 2012 by the American Physical Society.

of the LCO period, the pressure gradient driven part gradually increases. At the transition to the H-mode, the LCO disappears and only the pressure gradient driven part remains. The turbulence driven zonal flow assists the growth of the pressure gradient driven mean radial electric field by regulating the turbulent transport in the LCO phase, as predicted in [28]. This is regarded as a synergetic relation between the zonal flow and the pressure gradient driven mean radial electric field. A similar discussion of zonal flow production was addressed at the L–H transition that involves no LCOs [50, 71–74]. It was stated that the turbulence is quenched when the zonal flow production rate exceeds the effective growth rate of turbulence. A detailed parameter scan experiment for examining the role of the Reynolds stress driven radial electric field was recently performed in DIII-D [75].

Another example of the mean flow generation mediated by turbulence dynamics was reported in the LCO involving the high frequency branch of the zonal flow, the geodesic acoustic mode (GAM), in ASDEX-Upgrade [58]. Figure 6 compares the mean part of the shearing rate (τ_M^{-1}), the oscillating part of the shearing rate (τ_O^{-1}), and the turbulence decorrelation rate (τ_c^{-1}). In the I-phase, which refers to the time period in which the LCO emerges, the oscillating part of the shearing rate dominates over the mean part, and behaves very similar to the turbulence decorrelation rate. This means that the turbulence activity is regulated by the GAM during the I-phase. Meanwhile, the mean part of the shearing rate is gradually enhanced. Across the I-phase to H-mode transition, the mean part of the shearing rate eventually turns over the oscillating part, and limits the turbulence amplitude growth. With the assistance of the turbulence driven part of the radial electric field that can vary with a fast time scale such as the LCO frequency, the transport barrier can be developed by the gradient driven part of the radial electric field with its own time scale.

Recently, edge transport barrier formation was successfully reproduced using a first-principles-based global electrostatic gyrokinetic code, XGC1, in a realistic edge geometry of tokamak plasmas [76, 77]. In this study, it is proposed that the synergism between the Reynolds force and the ion orbit loss force comprehensively explains the time evolution of the shear flow structure formation, as shown in figure 7. The edge transport barrier formation is forced to occur by applying a sufficiently high heating input. Bifurcation is initiated by the oscillating fluid Reynolds force that induces the GAM at the edge, as shown in figure 7(*a*). The GAM seems to mitigate the turbulent transport that results in the edge temperature growth. As a result, the ion orbit loss force gradually grows and finally overtakes the Reynolds force (figure 7(*b*)). In the final stage of transport barrier formation, the sheared radial electric field structure is maintained by the ion orbit loss force that can endure even after the turbulence is quenched.

In the situation where the transition time scale is not very fast, it was demonstrated that the neoclassical process can solely account for the radial electric field excitation [64, 78]. In ASDEX-Upgrade, the diamagnetic velocity was found to approximately meet the spectroscopically measured $E \times B$ velocity oscillation in the LCO phase, as shown in figure 8 [64]. The authors claimed that the neoclassical contribution dominates over other factors. Insufficient drive of the fluid flow by the Reynolds force in the LCO phase was also pointed out in NSTX [79]. In the fluid simulation EMEDGE3D, the bulk part of the $E \times B$ flow kinetic energy was supplied by the neoclassical force (figure 9) [78]. In this case, the Reynolds force is responsible for both the high frequency fluctuation and for the sink of the macroscopic flow. According to the classification by Terry [19], these observations are grouped into the two-step transition, where the radial electric field is maintained by turbulence-force-free bifurcation mechanisms, and

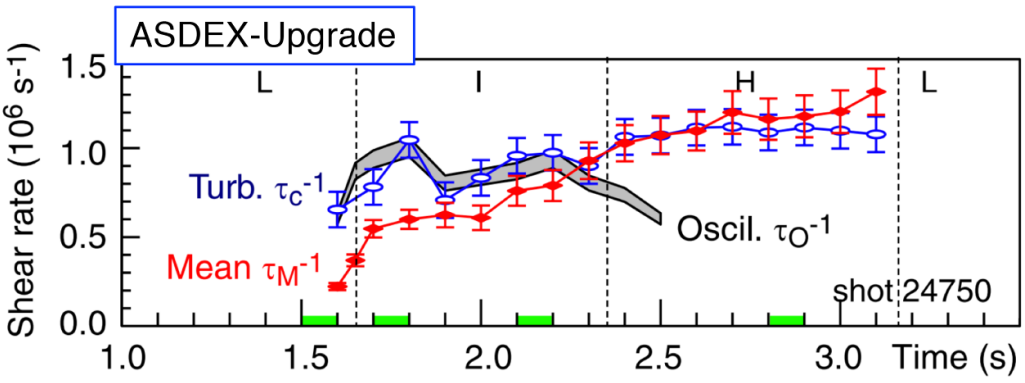

Figure 6. Time evolution of the mean and oscillating radial electric field shearing rates and the turbulence decorrelation rate. Reprinted figure with permission from [58], Copyright 2011 by the American Physical Society.

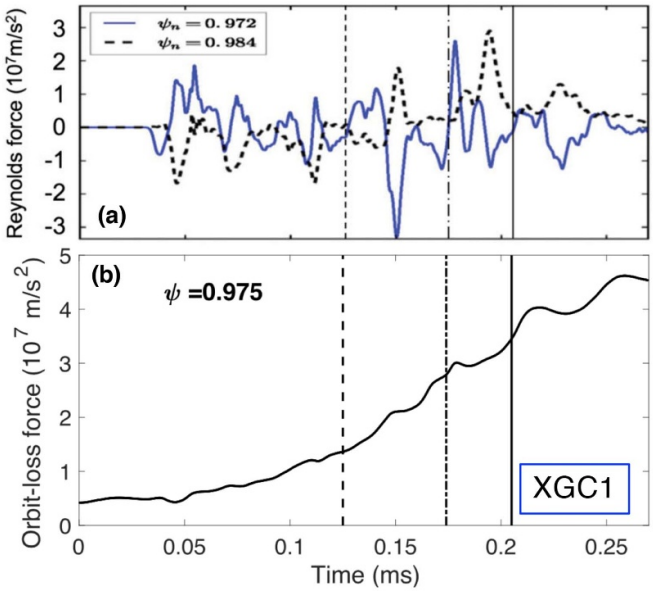

Figure 7. Time evolution of (*a*) the Reynolds force and (*b*) the orbit loss force across the edge transport barrier formation. Reprinted figure with permission from [76], Copyright 2017 by the American Physical Society.

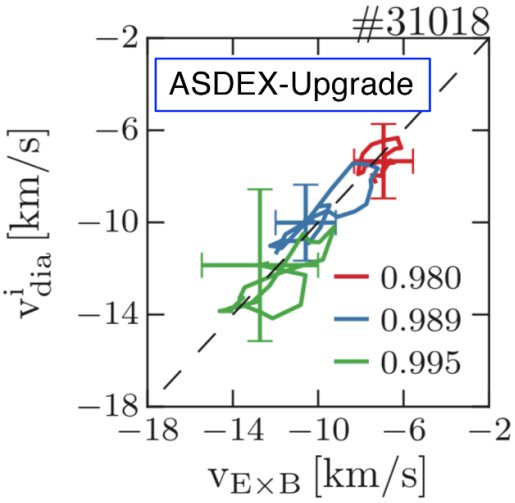

Figure 8. Relation between the $E \times B$ velocity and the diamagnetic velocity at three different radial positions in the limit cycle oscillation period. Reproduced courtesy of IAEA. Figure from [64]. © 2017 EURATOM.

the turbulence suppression by the excited radial electric field structure occurs afterwards.

A different aspect of the LCOs, their strong magnetic fluctuation nature, attracts much attention. A coherent poloidal field fluctuation in LCO was reported in ASDEX-Upgrade and other devices [65–67]. These observations share a unique characteristic of the oscillating spatial structure, that is the up-down asymmetric $m = 1$ magnetic oscillation, where m is the poloidal mode number of the oscillation. Figure 10 shows a schematic view of the the poloidal magnetic probe array and the time evolution of the poloidal magnetic field fluctuation in the LCO phase. The poloidal magnetic field oscillation is regarded as the parallel current oscillation. It was proposed that the up–down asymmetry of the parallel current oscillation can be explained by the Stringer spin-up mechanism [80]. A Lotka–Volterra-type set of equations that describes the system evolution can be obtained from that model, on which the LCO arises. The robustness of this interpretation is also shown by the fact that the experimentally measured LCO frequency agrees with the Stringer spin-up relaxation frequency. Another type of H-mode transition involving the LCO stimulated by a quasi-coherent electromagnetic oscillation was also reported in HL-2A [81]. Note that this type of coherent magnetic field oscillation is not always observed in LCO activity. For example, the case in [63] does not show a strong magnetic oscillation at the LCO frequency.

2.5. The role of the relative dielectric constant in toroidal plasmas in quantitative model validation

For the quantitative model validation based on the equation of motion or the current equation (6), it is essential to consider what model should be used as the relative dielectric constant in toroidal plasmas, $\epsilon_\perp$. The magnitude of $\epsilon_\perp$ can be derived as follows [3]: Starting from a cylindrical geometry with the confinement magnetic field B in the axial direction, the time

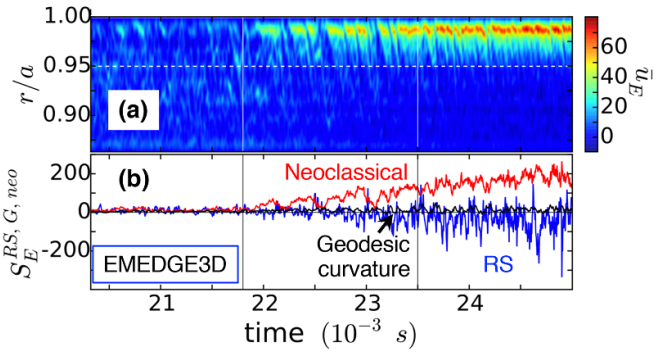

Figure 9. (*a*) Spatiotemporal evolution of the edge $E \times B$ velocity and (*b*) time evolution of the different energy sources of the $E \times B$ flow. Reproduced courtesy of IAEA. Figure from [78]. Copyright 2015 IAEA.

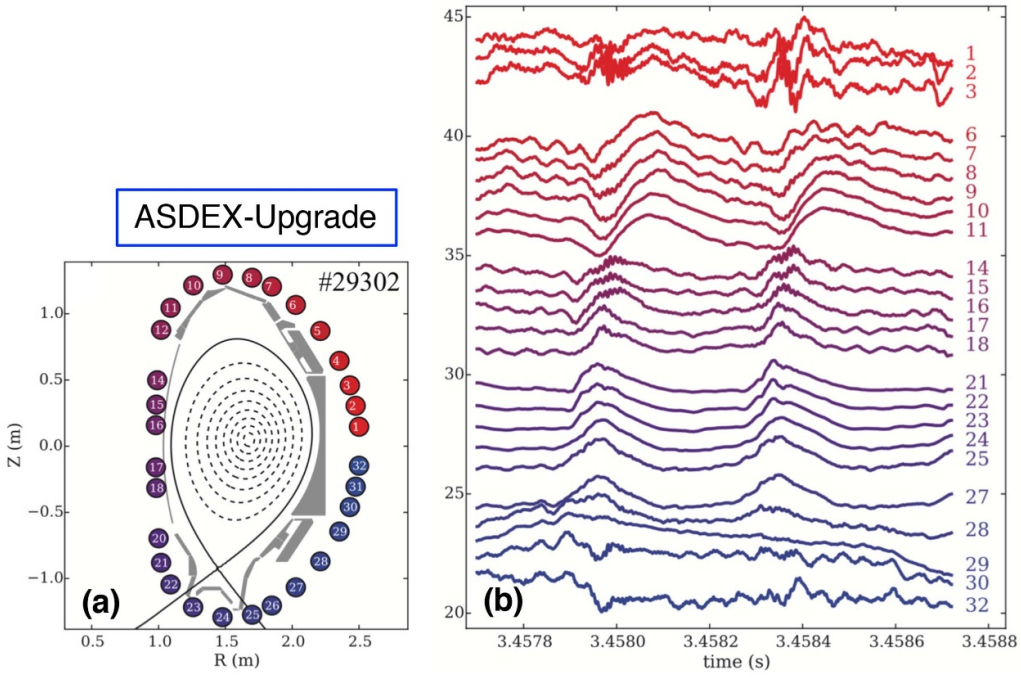

Figure 10. (*a*) Schematic view of the the poloidal magnetic probe array and (*b*) time evolution of the magnetic field fluctuation at the LCO phase. The probe locations in (*a*) and the signals in (*b*) are related by different colors and labels on the curves. Reproduced courtesy of IAEA. Figure from [65]. © 2016 EURATOM.

varying radial electric field causes the polarization current

$$J_{\rm pol} = \frac{nm}{B^2}\frac{\partial E_r}{\partial t}. \tag{10}$$

The polarization current shields the growth of the radial electric field on the one hand, and drives the $E_r \times B$ poloidal flow by the $J_{\rm pol} \times B$ force on the other hand. Assuming that E_r and $J_{\rm pol}$ are constant on the equiradial surface, a combination of Gauss's law and the charge continuity equation gives

$$-\epsilon_0 \frac{\partial E_r}{\partial t} = J_{\rm pol} + \sum J, \tag{11}$$

where $\sum J$ corresponds to the sum of the radial currents that induce the radial charge separation, i.e. the right hand side of equation (6) in the case of toroidal geometry. Substituting equation (10) into equation (11) gives

$$-\epsilon_\perp \epsilon_0 \frac{\partial E_r}{\partial t} = \sum J \tag{12}$$

with the relative dielectric constant for cylindrical plasmas

$$\epsilon_\perp = 1 + \frac{c^2}{v_{\rm A}^2}, \tag{13}$$

where $v_{\rm A} = B/\sqrt{nm\mu_0}$ is the Alfvén speed. According to [30–33, 82], in toroidal plasmas the effective mass of the ion fluid is enhanced by

$$M_{\rm tor} = 1 + \frac{1.6q^2}{\sqrt{\epsilon_\perp}} \tag{14}$$

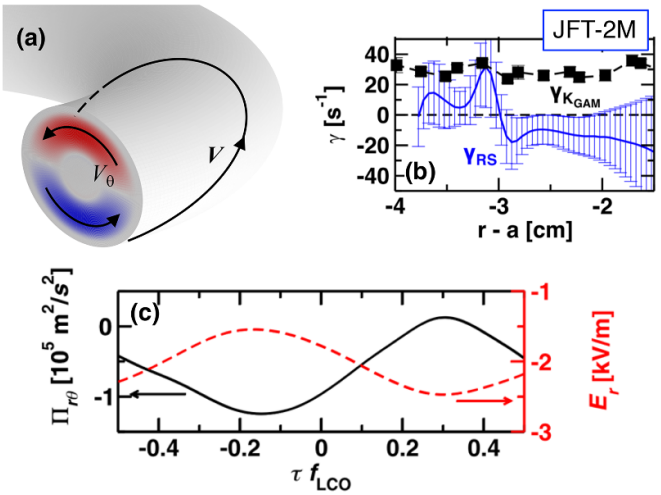

Figure 11. The role of the relative dielectric constant in toroidal plasmas for poloidal flow excitation: (*a*) illustration of poloidal flow and toroidal flow coupling via the finite divergence, (*b*) the radial profile of the GAM excitation rate by the Reynolds stress (γ_{RS}, blue) and that directly fitted by the GAM fluctuation energy ($\gamma_{K_{GAM}}$, black), and (*c*) the time evolution of the Reynolds stress and the radial electric field during the LCO phase. (*b*) Reprinted figure with permission from [86], Copyright 2018 by the American Physical Society. (*c*) Reprinted figure with permission from [62], Copyright 2013 by the American Physical Society.

in the banana regime and by

$$M_{\rm tor} = 1 + 2q^2 \tag{15}$$

in the plateau regime. Typically in the tokamak edge, $M_{\rm tor} \sim O(10)$ due to $q \gg 1$. The relative dielectric constant of the toroidal plasma becomes

$$\epsilon_\perp = 1 + M_{\rm tor}\frac{c^2}{v_{\rm A}^2}. \tag{16}$$

The cause of the inertia enhancement is the finite divergence of the poloidal flow in the toroidal plasma, i.e. $\nabla \cdot \mathbf{V}_\perp = -2\,{\rm R}^{-1}\sin\theta V_\theta$ [31]. When the flow frequency is much smaller than the GAM frequency, $\omega \ll \omega_{\rm GAM}$, this finite divergence is compensated by the toroidal return flow along the magnetic field line, $V_{||} = 2q\cos\theta V_\theta$. The up–down asymmetric poloidal flow divergence and the streamlines of the poloidal flow and the return flow are illustrated in figure 11(*a*). As a result, the poloidal momentum is transferred into the toroidal momentum, which leads to the enhanced effective inertia. In the high frequency regime $\omega \sim \omega_{\rm GAM}$, the poloidal flow divergence can be the up–down asymmetric density perturbation of the GAM. A stationary toroidal flow that has a fundamental feature of the toroidal return flow is actually observed in different devices [44, 83].

The importance of the finite inertia enhancement in equation (14) or equation (15) for the relative dielectric constant in toroidal plasmas is quantitatively presented using data for the GAM dynamics [84, 85] and those of the LCO dynamics [62, 63] in JFT-2M. Figure 11(*b*) shows the radial profile of the GAM excitation rate by the Reynolds stress and that directly obtained by the rising time scale of the GAM fluctuation energy [86]. Here the horizontal axis corresponds to the radial distance from the last closed flux surface, $r-a$. At $r-a \sim -3$ cm, two excitation rates independently obtained overlap, showing that the Reynolds stress plays the major role in the GAM excitation at this location. Here, the GAM driving force by the Reynolds stress is estimated based on the equation of motion with no inertia enhancement, i.e. $M_{\rm tor} = 1$, since the time scale of interest is high enough, $\omega \sim \omega_{\rm GAM}$ [87]. This observation implies that the estimation of the absolute value of the Reynolds stress is valid.

In the same discharge, the GAM disappears and the LCO takes over in a few hundred milliseconds before the L–H transition. Note that LCO with a small amplitude, and therefore not involving transitions to the deep H-mode, is sometimes specifically called 'small amplitude LCO' (SALCO) [70]. The LCO activity in JFT-2M [62, 63], as described in detail below, can be defined as SALCO. In the LCO phase, oscillations in the $E\times B$ velocity and the Reynolds stress at a nearly constant frequency are observed. Figure 11(*c*) shows the conditionally averaged waveform in these quantities [62]. The equation of motion with the inertia enhancement factor takes the form $M_{\rm tor}mn\partial\hat{V}_{E\times B}/\partial t = -mnr^{-1}\partial r\hat{\Pi}_{r\theta}/\partial r + \cdots$, where $\cdots$ indicates additional effects, such as the collisional damping term [21]. The expected oscillatory $E\times B$ velocity, which is induced by the oscillatory Reynolds stress at the angular frequency of $\omega_{\rm LCO}$, is evaluated as $\delta|\hat{V}_{E\times B}| \sim |\hat{\Pi}_{r\theta}|L^{-1}M_{\rm tor}^{-1}\omega_{\rm LCO}^{-1}$, where L is the scale length of the Reynolds stress change. Substituting parameters $|\hat{\Pi}_{r\theta}|L^{-1} \sim 7\times10^6$ m/s^2, $\omega_{\rm LCO} \sim 3\times10^4$ s^{-1}, $L\sim1$ cm, and $M_{\rm tor} \sim 20$ for $q\sim3$ provides the expected amplitude of modulation $\delta|\hat{V}_{E\times B}| \sim 15$ m s^{-1}. Since the modulation amplitude of the $E\times B$ velocity in the LCO is $\sim$500 m s^{-1}, the Reynolds stress driven part is only a minor contribution to the total flow modulation. Instead, if $M_{\rm tor} = 1$ is used, the conclusion completely reverses: $\delta|\hat{V}_{E\times B}| \sim 300$ m s^{-1} is obtained so the Reynolds stress driven part will account for the bulk part of the oscillatory $E\times B$ velocity in the LCO.

This inertia enhancement effect is quantitatively assessed by a fluid-type transport code, showing the validity of the model described above [88]. Figure 12 shows the time evolutions of the radial electric field driven by the radial current of the high-energy ion transport. The simulations were run both in the toroidal geometry and in the cylindrical geometry to examine the impact of the toroidicity on the inertia enhancement effect. In the toroidal geometry, the time constant of the radial electric field variation is much larger compared to the cylindrical case. This is due to a large relative dielectric constant at a finite q value of $\sim$1.1 at the mid-radius, where a finite inertia enhancement of $1+2q^2 \sim 3.63$ is anticipated for the toroidal geometry case. The simulation shows that the time constant in the toroidal geometry is 3.59 times larger than that in the cylindrical geometry case, confirming the necessity of taking into account the neoclassical inertia enhancement factor in the relative dielectric constant.

As discussed in [21], the poloidal flow divergence can also be compensated by the radial flow. Direct measurement of the relative dielectric constant in toroidal plasmas might be challenging but it is highly desirable for validating the model of the inertia enhancement factor.

2.6. Discussion

In this paper, a variety of radial electric field excitation mechanisms were described, considering possible combinations of different concepts. The interpretations of these examples are fairly case dependent, and to pursue a comprehensive model the detailed comparison and unification of different case studies are essential. As a first step, the phenomenological classification of essential mechanisms in different parameter ranges, e.g. below or above the bottom density point in the rolling-over L–H power threshold diagram or the isotope mass dependent threshold power [49, 50], seems to provide a perspective.

Considering the fact that the radial electric field settles on the neoclassical value [45, 48], a fundamental question arises. As shown in [45], the net fluid flow, which is the sum of the $E\times B$ flow and the ion diamagnetic flow, stays at rest in the H-mode. Indeed, the $E\times B$ flow of the neoclassical radial electric field is expected to be of a similar magnitude to the ion diamagnetic flow but directed towards the electron diamagnetic direction. For the turbulence suppression, equivalent but sign independent roles of the $E\times B$ flow and the ion diamagnetic flow are considered, which makes both flows effective [89]. In a different model, the impact of the electron diamagnetic effect on the turbulence linear growth rate is discussed [90]. Critical investigation through experiments or numerical simulations of this issue is anticipated in the future for further understanding of the role of the radial electric field in turbulent transport suppression.

3. Turbulence transport suppression mechanism

This section is initiated by discussing the limitations of the shear-amplitude suppression paradigm addressed in a pioneering work in DIII-D [43]. Motivated by the necessity for new ingredients, recent experimental and theoretical results focusing on the important roles of the turbulence cross phase and the turbulence spatial redistribution induced by the radial electric field non-uniformity are presented to push the physical understanding beyond the paradigm.

3.1. Limitations of the shear-amplitude suppression paradigm

As the turbulent transport regulation mechanism in the H-mode, turbulence amplitude suppression by radial electric field shear is acknowledged as being of major importance [17]. However, there are some counterexamples showing the limitations of the shear-amplitude suppression paradigm. For example, figure 13(a) shows the radial profile of the relative turbulence amplitude in the Ohmic H-mode phase from the Ohmic phase. It is defined as $\tilde{I}(\mathrm{H})/\tilde{I}(\mathrm{OH})$, where $\tilde{I}(\mathrm{H})$ and $\tilde{I}(\mathrm{OH})$ are the turbulence amplitudes of any quantity in the Ohmic H-mode phase and the Ohmic phase, respectively. Circles and triangles correspond to plots for the density fluctuation and the potential fluctuation, respectively. The solid curve shows the radial electric field profile where the red shaded area indicates the E_r-well bottom region. Figure 13(b) shows the particle flux profile. Focusing on the radial electric field shear region, i.e. both sides of the E_r-well bottom, both the density fluctuation amplitude and the potential fluctuation amplitude are significantly reduced, which results in the transport suppression. However, at the E_r-well bottom, the density fluctuation amplitude reduction is only modest, and the potential fluctuation is even amplified. Even though the fluctuation amplitude reduction is not substantial, the particle flux can be reduced through the cross phase alternation, since the turbulent particle flux is defined in the form of

$$\Gamma_r = B^{-1}|\tilde{n}||\tilde{\phi}|\gamma_{n\phi}k_\theta \sin\alpha_{n\phi}, \tag{17}$$

where $|\tilde{n}|$, $|\tilde{\phi}|$, $\gamma_{n\phi}$, $\alpha_{n\phi}$, and k_θ denote the density fluctuation amplitude, the potential fluctuation amplitude, the cross coherence and the cross phase between them, and the poloidal wavenumber, respectively [91]. Looking at figures 13(c) and (d), it is found that the particle flux quench after the H-mode transition at the E_r-well bottom region is attributed to the cross phase alternation. The cross phase effect seems to be more essential in particular at a location where the radial electric field shear is not remarkably strong. Experimental activities focusing on the cross phase were also reported for different toroidal plasmas [92–94]. In early studies, the impact of the sheared radial electric field on both the fluctuation amplitude and the cross phase were theoretically modelled [89, 95] and the experimental validation of these models was performed in a basic experimental device [96, 97]. In this paper, the importance of the cross phase behavior is addressed from another aspect, that is the decoupled dynamics of the cross phase with respect to the amplitude evolution, which has lately been discussed experimentally and theoretically.

In the presence of a non-uniform radial electric field structure, it is anticipated that the mutual nonlinear interaction between the radial electric field and the turbulence results in a spatial redistribution of the turbulence profile.

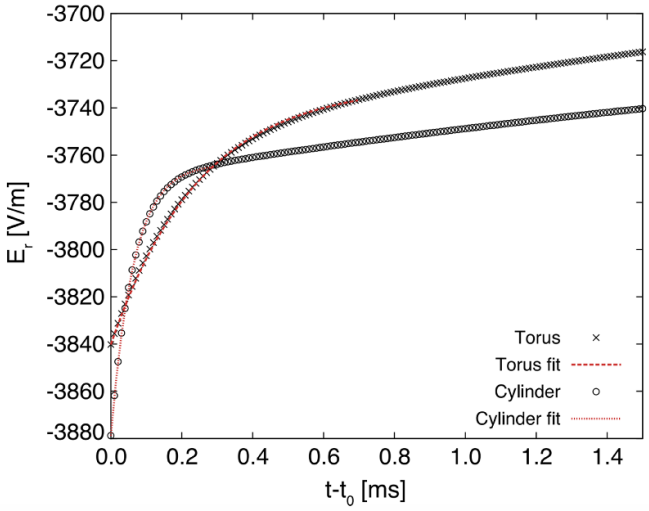

Figure 12. Time evolution of the radial electric field driven by the fast ion radial current in the toroidal geometry and the cylindrical geometry. Reprinted from [88], Copyright 2016, with permission from Elsevier.

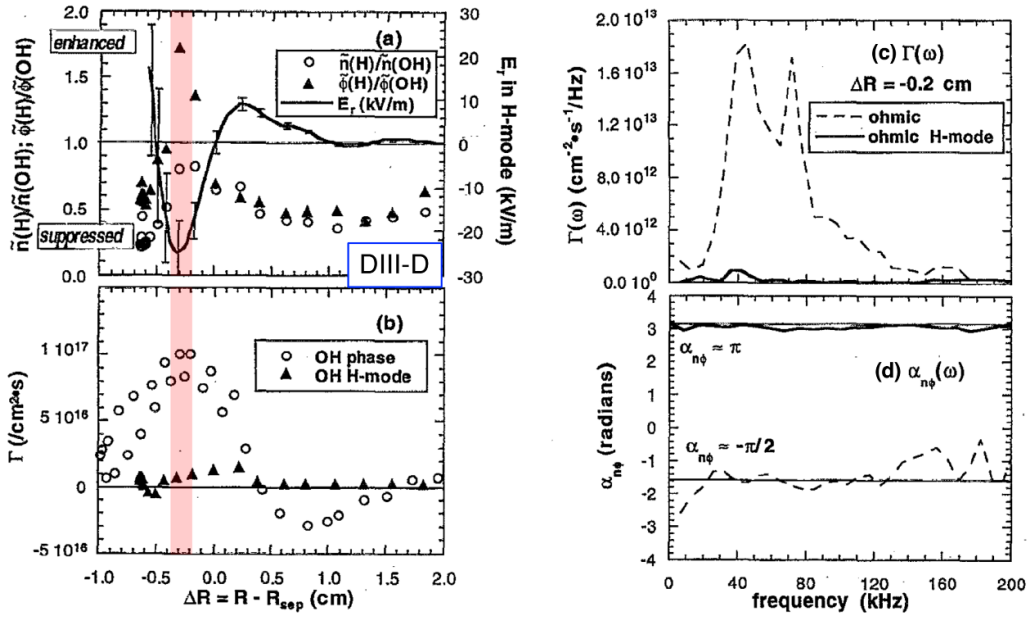

Figure 13. Radial profiles of (*a*) the radial electric field and the relative turbulence amplitude in the density fluctuation and the potential fluctuation with respect to the values in the Ohmic phase and (*b*) the particle flux. Frequency decomposed spectrum of (*c*) the particle flux and (*d*) the cross phase between the density fluctuation and the potential fluctuation. Reprinted from [43], with the permission of AIP Publishing.

Since the E_r-well structure has both the shear region and the curvature region, the different roles of those structures on the turbulent transport regulation are investigated intensively [41, 98, 99]. Moreover, it is predicted that radially propagating radial electric field structures such as the zonal flows or the GAMs can lead to the spatial transmission of a turbulence clump, as reported in a the global gyrokinetic simulation code GYSELA [100]. Figure 14 shows the spatiotemporal evolution of the turbulence diffusivity in the presence of an energetic particle source. There are three different phases in the system evolution: (A) the energetic particle source is applied to a quasi-stationary turbulence regime, (B) a transport barrier is triggered at $r/a > 0.5$, and (C) nonlinear interaction between the energetic particle driven GAMs (EGAMs) and turbulence occurs. In particular, in phase (C), the turbulence clump penetrates into the transport barrier region because a portion of the turbulence is trapped by the radially propagating EGAMs.

Note that some previous models, including the predator–prey model, are based on the spatial integration in the scale of the radial electric field structure. Therefore neither the different roles of the shear and curvature of the radial electric field nor the turbulence trapping by the radial electric field structure can be treated in those frameworks. To overcome those points, a new theoretical mode that is not based on spatial integration was developed recently [101, 102]. In this model, the interaction between the radial electric field and turbulence is locally

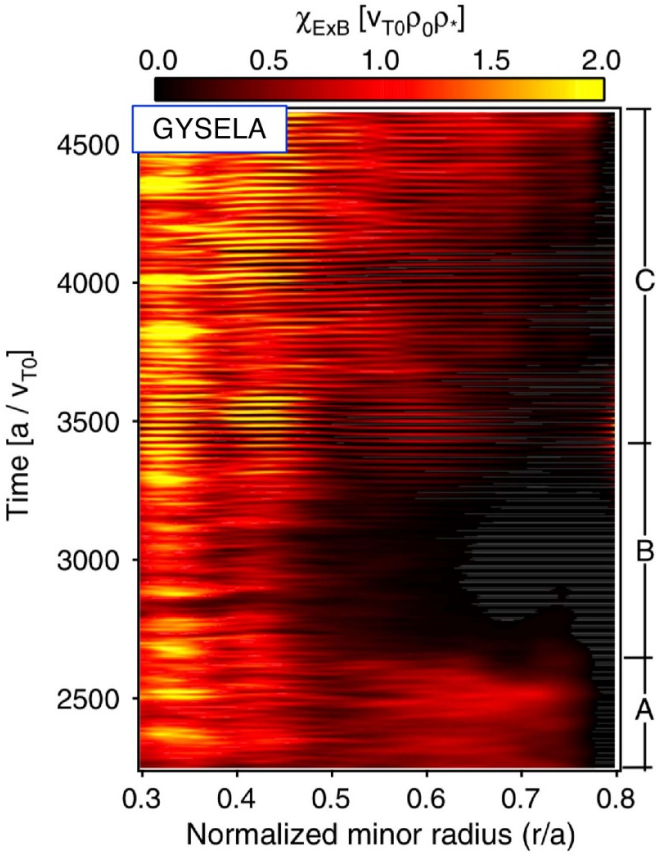

Figure 14. Spatiotemporal evolutions of turbulence diffusivity. Reprinted figure with permission from [100], Copyright 2013 by the American Physical Society.

described so that the turbulence trapping can be treated. Often, experimental model validation is based on the local measurement of the radial electric field and the turbulence. Therefore a spatially non-integrated model might better describe the experimental situation. In the subsection below, newly obtained understanding based on this model is discussed.

3.2. Decoupled dynamics of the cross phase from the amplitude evolution

One of the interesting results was reported from the TJ-K stellarator experiment [103]. In this device, a pair of 64-pin poloidal Langmuir probe arrays is installed in two different toroidal sections to simultaneously measure the fine structure of the zonal flow and the turbulent transport. One of the probe arrays is shown in figure 15(*a*). By using these probe arrays, the zonal average can be performed for the particle flux oscillation and the potential oscillation, from which the interaction between the net particle flux and the zonal potential can be discussed. Figure 15(*b*) is the conditionally averaged time evolution of the global particle flux variation and the zonal potential. Before the zonal potential bursts, the turbulence particle flux increases to nonlinearly drive the zonal potential. At the moment of the zonal potential burst the particle flux is suppressed, and the state of the suppressed particle flux continues for ∼0.1 ms even after the zonal potential returns back to the original level.

In order to decompose the contributions of each factor in equation (17), the wavenumber spectra of the ion saturation current fluctuation, the potential fluctuation, the particle flux, and the cross phase between the density fluctuation and the poloidal electric field fluctuation are shown in figures 15(*c*)–(*f*), respectively. Note that the $\pi/2$ cross phase between the density fluctuation and the poloidal electric field fluctuation makes the particle flux zero, because the phases of the poloidal electric field and the potential differ by $\pi/2$. The cross coherence between the density fluctuation and the poloidal electric field fluctuation changes only little, thus is not shown here. Before the zonal potential bursts, the turbulence amplitudes in both the ion saturation current fluctuation and the potential fluctuation increase, which results in increased particle flux. The cross phase also changes to enhance the particle flux. At the time instant of the zonal potential burst, the turbulence amplitudes stay at the averaged values and do not contribute to a particle flux change. Meanwhile, the cross phase approaches $\pi/2$, playing the main role in the particle flux suppression in this time period. After the zonal potential burst ceases, all components behave to reduce the particle flux that keeps the particle flux level lower compared to the averaged value. Overall, the cross phase responds to the zonal potential variation prior to the turbulence amplitude.

Another example showing the decoupled dynamics between the cross phase and the turbulence amplitude was reported from the JFT-2M tokamak experiment [104]. Figure 16 shows the time evolutions of the radial electric field, the relative density fluctuation amplitude, the cross phase between the density fluctuation and the potential fluctuation, and the particle flux measured at the E_r-well bottom across the L–H transition. Here, the particle flux disappears when the cross phase between the density fluctuation and the potential fluctuation is zero. The poloidal wavenumber of the turbulence is also moderately reduced across the L–H transition, contributing a further transport reduction. In order to avoid a large uncertainty brought about by the poloidal wavenumber evolution, the poloidal wavenumber in the L-mode is used here to obtain the time evolving particle flux using equation (17). Therefore, the value in figure 16(*d*) corresponds to the possible upper boundary of the particle flux. Immediately after the radial electric field grows negatively, the density fluctuation amplitude quickly responds with the time scale of O(0.1 ms). A prompt reduction of the particle flux is brought about by this amplitude reduction of the turbulent density fluctuation. However, the density fluctuation amplitude quickly recovers afterwards, and its net reduction is only moderate. Meanwhile, the cross phase between the density fluctuation and the potential fluctuation changes slowly with the time scale of O(1 ms). In the later phase, where the density fluctuation amplitude level recovers, the particle flux remains reduced thanks to the cross phase reduction. Clear time scale separation between the amplitude suppression and the cross phase reduction implies the existence of different

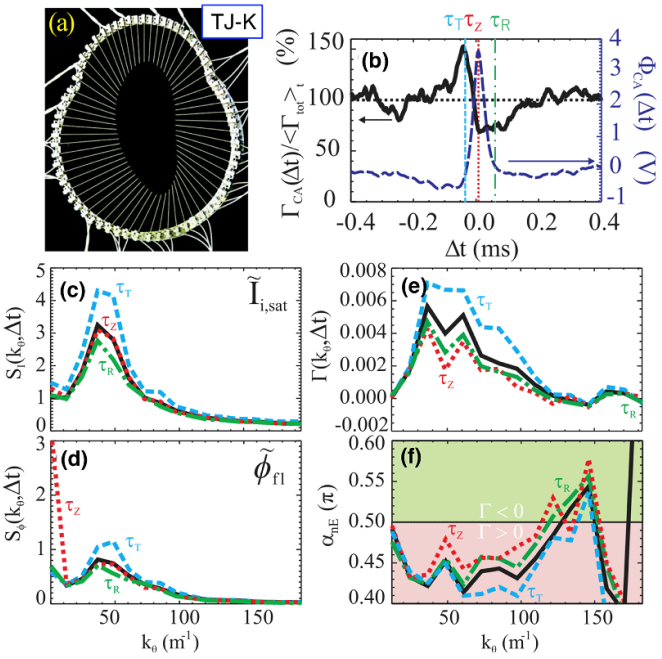

Figure 15. (*a*) Schematic view of the poloidal Langmuir probe array, (*b*) the conditionally averaged time evolution of the particle flux variation and the zonal potential, (*c*)–(*f*) the wavenumber spectra of the ion saturation current fluctuation, the potential fluctuation, the particle flux, and the cross phase, respectively. In (*c*)–(*f*), the black curve shows the averaged spectra and the curves with different color correspond to the spectra at the time instance indicated by the vertical lines in (*b*). Reprinted figure with permission from [103], Copyright 2013 by the American Physical Society.

underlying mechanisms. In particular, the turbulence amplitude is determined by nonlinear saturation, while the cross phase is equivalent to the source of the linear instability, i.e. the incomplete adiabatic response of electrons with respect to the potential fluctuation in the case of the resistive drift wave. Curiously, the order of changes here is opposite to the case of TJ-K, in which the cross phase responds prior to the fluctuation amplitude.

Further discussion of the turbulence particle flux reduction in JFT-2M concerns its spatial distribution. Figure 17 shows the radial profiles of the radial electric field, the particle flux, the relative density fluctuation amplitude, the potential fluctuation amplitude, and the cross phase between the density fluctuation and the potential fluctuation in the L-mode phase and in the H-mode phase. As shown in figure 17(*b*), the turbulent particle flux is reduced in a wide radial region. The different role of the radial electric field non-uniformity is explored by dividing the entire peripheral region into sub-regions. The two regions with green shading correspond to the inner shear region ($-2.2 < \mathrm{r} - \mathrm{a} < -1.5$ cm) and the outer shear region ($-0.5 < r - a < 0$ cm). In addition, there is the curvature region ($-1.5 < \mathrm{r} - \mathrm{a} < -0.5$ cm) indicated by the orange shading between these two shear regions. Moreover, a further inside region ($r - a < -2.2$ cm) is characterized by very low shear or curvature of the radial electric field. Across the L–H transition, the density fluctuation amplitude is substantially suppressed at both the inner shear region and the outer shear region, while the variation is only moderate in the curvature region. For the potential fluctuation amplitude, the reduction is visible only in the inner shear region. It approximately stays unchanged in the curvature region, and is even enhanced in the outer shear region. The cross phase approaches zero in the inner shear region and the curvature region, and in the outer shear region it becomes negative. Combinations of different components account for the overall particle flux suppression observed in a wide range of the radius.

Interestingly, in the further inside region, all the components behave so as to reduce the particle flux with very low shear or curvature of the radial electric field. A similar observation was reported in an early study [13]. The turbulence amplitude reduction at the region where the radial electric field structure is not substantially large can be explained by the turbulence spreading theory [105–107]. Experimental assessments of the turbulence spreading concept were recently reported [62, 108, 109]. The turbulence spreading is an important concept which is expected to explain a long-standing mystery, the prompt confinement improvement over a wide region of plasma at the L–H transition [14].

To understand the decoupled behavior of the turbulence amplitude and the cross phase a dynamic model was developed, as reported in [110]. Starting from the trapped electron mode (TEM) turbulence model [111], the following expression for the cross phase dynamics is obtained:

$$\frac{\partial \alpha_{n\phi,k}}{\partial t} = \left[1+\frac{3}{2}\eta_{\mathrm{e}}\right] k_y \beta_k \cos\alpha_{n\phi,k} - \omega_k - \nu\beta_k \sin\alpha_{n\phi,k} + I_{\mathrm{NL},k}, \tag{18}$$

where $\alpha_{n\phi,k}$ is the cross phase between the density fluctuation and the potential fluctuation, $\beta_k = |\phi_k|/|n_k|$ is the amplitude ratio of the potential fluctuation to the density fluctuation, ω_k is the fluctuation angular frequency, the subscription k indicates the wavenumber of interest, $\eta_{\mathrm{e}} = L_n/L_{T_{\mathrm{e}}}$ is the ratio of the

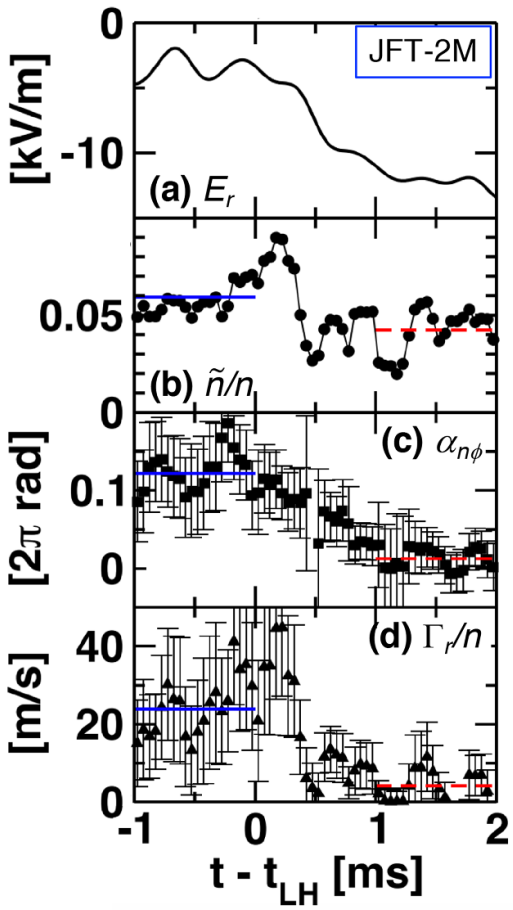

Figure 16. Time evolutions of (*a*) the radial electric field, (*b*) the relative density fluctuation amplitude, (*c*) the cross phase between the density fluctuation and the potential fluctuation, and (*d*) the particle flux measured at the E_r-well bottom across the L–H transition. Reproduced from [104]. CC BY 4.0.

density gradient length to the temperature gradient length, and ν is the de-trapping rate for trapped electrons. The nonlinear contribution due to the $E \times B$ advection is given as

$$I_{\mathrm{NL},k} = \frac{1}{|n_k|^2}\mathrm{Im}[n_k^*(v_E \cdot \nabla n)_k]. \tag{19}$$

Here, time and space are normalized by $\rho_s c_s^{-1}$ and ρ_s, respectively, where ρ_s is the ion sound gyro-radius and c_s is the ion sound speed.

Utilizing this model, the impact of the pump wave-zonal flow interaction on the cross phase of the pump wave is discussed. Figure 18(*a*) presents a diagram of the model framework. The situation considered in the model is as follows. First a pump TEM turbulence interacts with a linearly stable seed zonal flow that generates two sidebands. The sidebands couple with the pump TEM turbulence to nonlinearly drive the zonal flow. At the same time, the nonlinear interaction between the sidebands and the zonal flow occurs, which reacts back to the pump TEM turbulence. The LCO dynamics with and without considering the finite cross phase effect are plotted in figure 18(*b*). In the results of the simulation, a decoupled dynamics of the pump TEM wave amplitude and the cross phase is demonstrated as a trajectory that is not on a flat plane.

3.3. *Turbulence spatial redistribution induced by the radial electric field non-uniformity*

A model for the dynamic interaction between the radial electric field structure and the turbulence was developed [101, 102] in the framework of the wave kinetic theory [112]. Aiming at treating the turbulence trapped by the radial electric field structure, the phase-space dynamics of the turbulence is accounted for. The evolution of turbulence can be described by

$$\frac{\partial \mathcal{N}_k}{\partial t} + \{\omega_k, \mathcal{N}_k\} = \gamma_{\mathrm{L}}\mathcal{N}_k - \Delta\omega\mathcal{N}_k^2, \tag{20}$$

where $\mathcal{N}_k$ is the dimensionless wave action density, ω_k is the turbulence angular frequency, γ_{L} is the linear growth rate, and $\Delta\omega$ is the nonlinear decorrelation rate. Here, time and space are normalized by $\rho_s V_{\mathrm{d}}^{-1}$ and ρ_s, respectively, where V_{d} is the diamagnetic drift velocity. In particular for the drift wave turbulence, $\mathcal{N}_k$ and ω_k are given as

$$\mathcal{N}_k = (1 + k_x^2 + k_y^2)^2|\phi_k|^2, \tag{21}$$

and

$$\omega_k = \frac{k_y}{1 + k_x^2 + k_y^2} + k_y\hat{V}_y, \tag{22}$$

respectively, where k_x is the radial wavenumber, k_y is the poloidal wavenumber, ϕ_k is the normalized turbulence electrostatic potential, and $\hat{V}_y$ is the poloidal velocity modulation in a macro–or meso-scopic $E \times B$ flow structure. In the nonlinear saturation phase of the turbulence, i.e. $\gamma_{\mathrm{L}}\mathcal{N}_k - \Delta\omega\mathcal{N}_k^2 = 0$, the equi-frequency plane in the phase-space corresponds to the constant of motion. In the presence of the $E \times B$ flow structure, the turbulence frequency contour in the phase-space is distorted by the Doppler shift and then the turbulence trapping occurs.

Two applications of the wave kinetic theory for the interaction between the turbulence and the EGAM [101] and that between the turbulence and the turbulence driven GAM [102] are demonstrated in the rest of this subsection. The schematic view of the former case is given in figure 19(*a*). The turbulence is set to be unstable only on the left side of the simulation region, while a stationary mean flow structure that stabilizes the turbulence is placed in the rest of the region. An EGAM propagating radially outward is applied externally . Note that the energy exchange between the EGAM and the turbulence need not be considered since the EGAM is not excited by the turbulence, which simplifies the situation. The result of the numerical examination of the model is shown in figure 19(*c*). Due to existence of the EGAM flow structure, the Doppler shifted turbulence frequency (white contour lines) has island structures in the phase-space, inside which the turbulence is trapped. Since the EGAM propagates radially outward, the trapped turbulence penetrates into the linearly stable

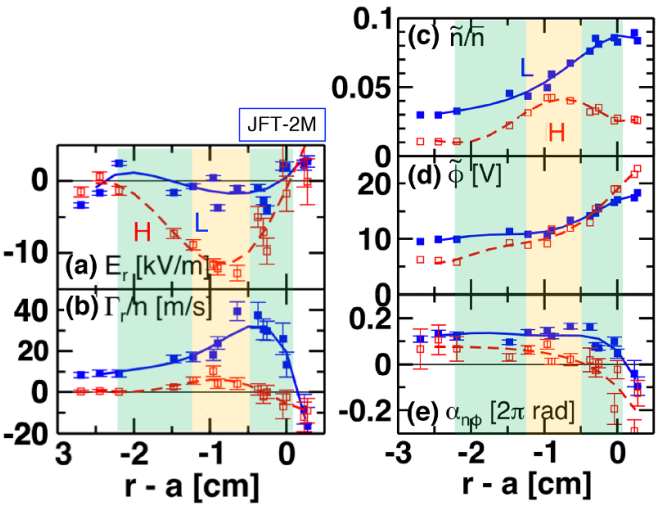

Figure 17. Radial profiles of (*a*) the radial electric field, (*b*) the particle flux, (*c*) the relative density fluctuation amplitude, (*d*) the potential fluctuation amplitude, and (*e*) the cross phase between the density fluctuation and the potential fluctuation in the L-mode phase and in the H-mode phase. Reproduced from [104]. CC BY 4.0.

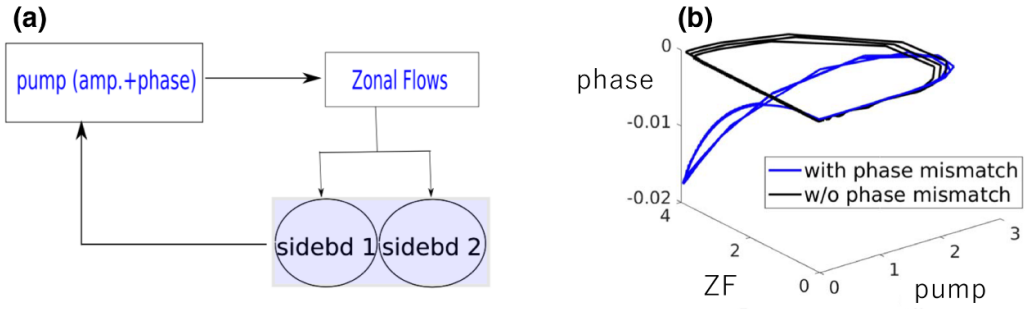

Figure 18. (*a*) Schematic diagram of the parametric interaction between the pump TEM turbulence, the zonal flow, and two sidebands, and (*b*) limit cycle oscillation between the pump wave amplitude, the zonal flow amplitude, and the cross phase. The blue and black curves show the models with and without the phase mismatch effect, respectively. Reproduced from [110].

region, $x > 20$. This concept of the turbulence trapping by the EGAM structure can give an explanation for the observation in the GYSELA simulation shown in phase (C) of figure 14. This result suggests that an attenuation of the transport barrier by the interaction between a radially propagating $E \times B$ flow structure and the turbulence is possible depending on the propagating direction.

A similar numerical investigation is performed for the turbulence driven GAM as well. In this case, the GAM excitation by the turbulence and the phase-space interaction between the GAM and the turbulence are simultaneously considered. The energy equations of the GAM and the turbulence are given as

$$\frac{\partial \hat{V}_y^2}{\partial t} = W_{\rm G} + 2\mu_{\rm G}\hat{V}_y\frac{\partial^2 \hat{V}_y}{\partial x^2}, \tag{23}$$

and

$$\frac{\partial \langle \mathcal{N}_k \rangle_k}{\partial t} + \frac{\partial}{\partial x}\langle v_{\rm g}\mathcal{N}_k\rangle_k = W_{\rm turb} + \langle \gamma_{\rm L}\mathcal{N}_k\rangle_k - \langle \Delta\omega\mathcal{N}_k^2\rangle_k \tag{24}$$

where $\mu_{\rm G}$ is the viscosity for the GAM, $v_{\rm g} \equiv \partial\omega_k/\partial k_x$ is the turbulence group velocity, and $\langle * \rangle_k \equiv \int *(1+k_x^2+k_y^2)^{-1}{\rm d}k_x$ is the wavenumber integration. The GAM energy gain and the turbulence energy loss are given as

$$W_{\rm G} = -2\hat{V}_y\frac{\partial \Pi_{xy}}{\partial x} \tag{25}$$

and

$$-W_{\rm turb} = -\left[\int \frac{2k_xk_y}{(1+k_x^2+k_y^2)^2}\mathcal{N}_k dk_x\right]\frac{\partial \hat{V}_y}{\partial x} = 2\Pi_{xy}\frac{\partial \hat{V}_y}{\partial x}, \tag{26}$$

where Π_{xy} is the fluid Reynolds stress. The simulation result in the GAM saturation phase is shown in figure 20, where the periodic boundary condition in the x direction is used. As shown in figure 20(*a*), the turbulence clump is trapped by the GAM at the location where the $E \times B$ flow is directed towards the electron diamagnetic drift direction. The energy exchange between the GAM and the turbulence is presented in figure 20(*b*). The GAM gains energy at which the curvature of the GAM is strong while the turbulence loses energy at which the $E \times B$ shear of the GAM is strong. Although the spatial distributions of $W_{\rm G}$ and $-W_{\rm turb}$ differ from each other, the spatially integrated energy budget balances between the GAM and the turbulence, i.e. $\int W_{\rm G}{\rm d}x = -\int W_{\rm turb}{\rm d}x$. The turbulence propagation rate is represented by the second term of the left hand side of equation (24), whose spatial distribution is shown

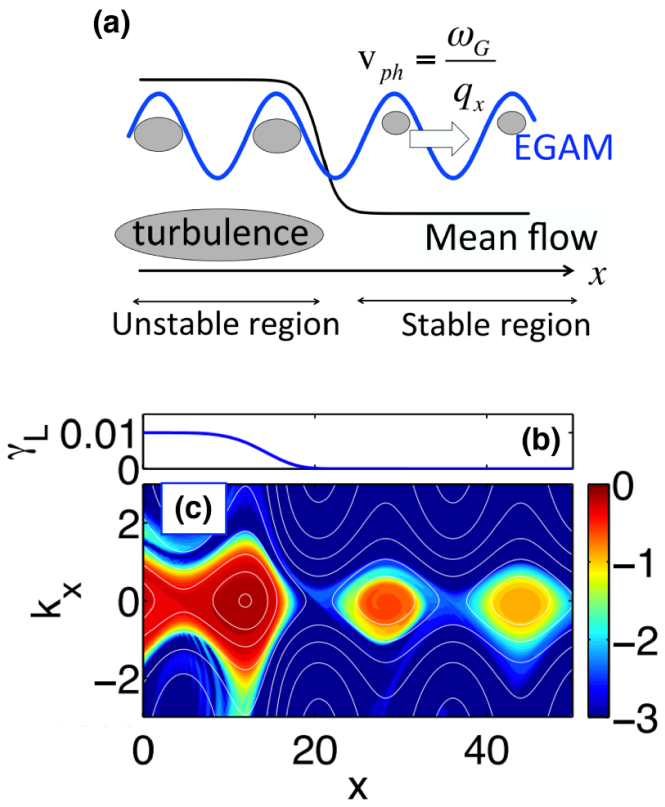

Figure 19. (*a*) Schematic view of the turbulence trapping by the EGAM in the presence of the transport barrier, (*b*) spatial profile of the turbulence linear growth rate, and (*c*) the phase-space distribution of the dimensionless turbulence action density and contour of the equi-frequency plane. Reproduced from [101]. CC BY 4.0.

in figure 20(*c*). Since the turbulence propagation rate and the energy exchange terms are in the same order of magnitude, all these terms are essential for predicting the turbulence spatial redistribution induced by the $E \times B$ flow structure. Note that the spatial integration of equations (23) and (24) provides the well-known predator–prey model [28], where the turbulence propagation rate term disappears. The turbulence trapping by the radial electric field structure is an explanation of the enhancement or the moderate reduction of the turbulence amplitude at the curvature region [43, 104, 113].

A similar approach using a different model was reported in [114]. Here, the Hasegawa-Wakatani fluid model [115] is used to describe the spatial redistribution of the drift wave turbulence in the presence of the enforced sinusoidal zonal flow structure. As shown in figure 21(*a*), in the case that the given zonal flow amplitude is large enough, the turbulence is localized where the zonal flow curvature is negatively maximum both in the linear growth phase and the nonlinear saturation phase of the turbulence. This result agrees with that obtained with the wave kinetic theory, as discussed above [101, 102]. Around the location where the zonal flow curvature is positively maximum, the cross phase between the density fluctuation and the potential fluctuation is negatively enhanced, which stabilizes the drift wave and drives the negative particle flux simultaneously.

Different roles of the shear and the curvature of the radial electric field for both the turbulence amplitude redistribution and the cross phase modification are found. Further investigation of the turbulent transport quench at the edge transport barrier region is an interesting direction to provide an interpretation for the detailed observation of the radial electric field and the particle flux in JFT-2M (figure 17) [104].

3.4. Discussion

The contrasting results from TJ-K [103] and JFT-2M [104] regarding the dynamics in the turbulence amplitude and the cross phase are an interesting topic for discussion. Recent numerical simulation works showed that the cross phase modification can occur due to the electromagnetic effect in a tokamak edge, which is a possible mechanism that can dynamically vary the cross phase. Even without a large $\beta \equiv \left(p/(B^2/2\mu_0^2)\right)$, the electromagnetic turbulence can play a role because of a large q or a large inverse scale length $L_\perp^{-1}$ at the tokamak edge, since the ratio of the electromagnetic part to the electrostatic part in the parallel electric field fluctuation is approximated as $\left(qRL_\perp^{-1}\right)^2\beta$ [116]. It is shown that as the electromagnetic effect becomes significant, the cross phase is gradually altered [117, 118]. Immediately after the L–H transition, the pedestal structure is quickly formed and the importance of the electromagnetic turbulence component can accordingly rise through an increase of $L_\perp^{-1}$. Superposition of the electrostatic fluctuation and the electromagnetic fluctuation can cause a complex time evolution of the turbulence amplitude and the cross phase that strongly depends on the edge plasma parameters. The impact of the electromagnetic fluctuation on the turbulence driven $E \times B$ flow is also discussed [119].

Recently, the parallel flow shear driven instability was investigated theoretically [120] as a candidate for the inward particle pinch mechanism in the type-III ELM dynamics [121]. As the free energy of the parallel flow shear driven turbulence is the toroidal return flow shear in the H-mode, which has been discussed in the subsection 2.5, the up-gradient particle flux can be driven without violating the law of entropy increase [122]. Intensive assessments of the elementary process of the parallel flow shear driven instability were conducted in a basic linear plasma device [123, 124]. This idea can be applied to consider the different time scale of the turbulence amplitude reduction and the cross phase alternation. Once the excited radial electric field at the L–H transition secondarily stimulates the parallel flow shear driven instability through the toroidal return flow, competition against the original instability is thought to occur. As a result, the cross phase is altered with a delayed time scale compared to the prompt turbulence amplitude suppression. Detailed practical assessment is left for future research.

4. Summary

In this special topic paper, recent progress on the role of the mean and oscillating radial electric field in the L–H transition was reviewed. It was shown that the radial electric field driving

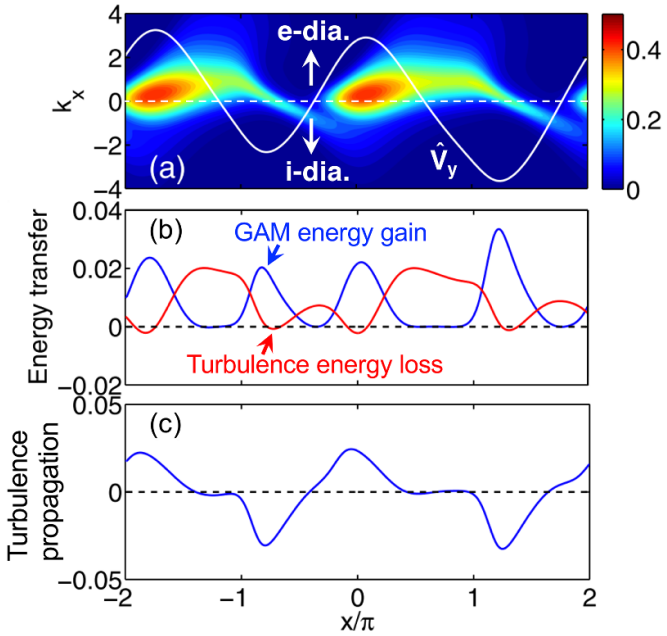

Figure 20. (*a*) Phase-space distribution of the dimensionless turbulence action density and (*b*) spatial distribution of the GAM waveform, and spatial profiles of (*c*) the GAM energy gain and the turbulence energy loss and (*d*) the turbulence propagation rate. Reprinted from [102], with the permission of AIP Publishing.

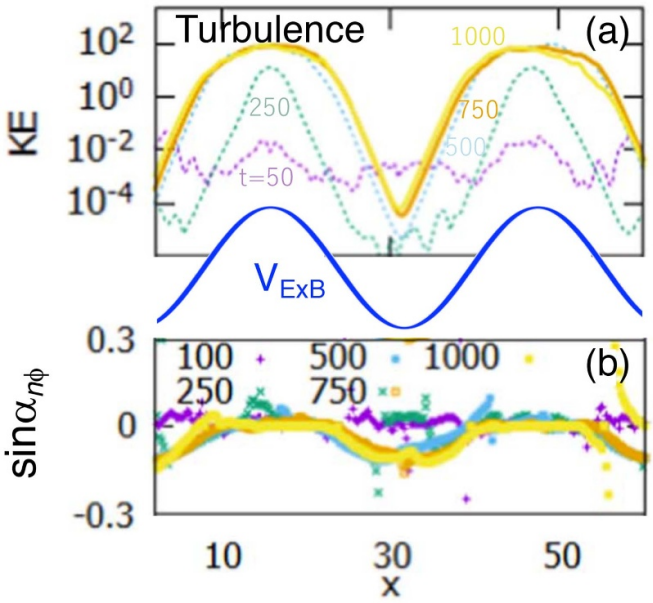

Figure 21. Spatial distributions of (*a*) the turbulence kinetic energy and (*b*) the sine of the cross phase between the density fluctuation and the potential fluctuation at different time instances in the presence of the enforced sinusoidal zonal flow. Reproduced from [114]. © IOP Publishing Ltd. All rights reserved.

procedure has apparent conflicting characteristics: the quick evolution in the turbulence time scale and the eventual settling on the diamagnetic value. These points were reconciled by combining different models of the radial electric field excitation based on the turbulence driven component and on the profile driven component.

Another point focused upon was the turbulent transport suppression mechanism. It was pointed out that the turbulence particle flux behavior in the presence of the well-shaped radial electric field structure cannot be fully featured by the shear-amplitude suppression paradigm. Two additional concepts were proposed, i.e. the cross phase alternation and the turbulence redistribution induced by the interaction with the radial electric field structure. In particular, the different time scales seen in the turbulence amplitude suppression and the cross phase alternation that impact on the particle flux behavior across the L–H transition were presented. A new modeling activity based on the wave kinetic framework that can treat the spatially decomposed turbulence–radial electric field interaction was introduced as a key concept to investigate the spatial redistribution of the turbulence in the H-mode.

Acknowledgment

The author would like to thank M. Sasaki, K. Ida, K. Itoh, the late S.-I. Itoh, T. Ido, K. Kamiya, Y. Kosuga, Z. Yan, J. Cheng, G.R. McKee, C. Bourdelle, H. Jhang, N. Aiba, S. Maeyama, M. Honda, T. Nishizawa, G. Birkenmeier, and C. Hidalgo for fruitful discussions and valuable input. This work is partly supported by a Grant-in-Aid for Scientific Research of Japan Society for the Promotion of Science (17K14898) and NIFS Library Publishing Committee.

ORCID iD

T. Kobayashi https://orcid.org/0000-0001-5669-1937

References

[1] Kaye S.M. *et al* 1997 *Nucl. Fusion* **37** 1303
[2] Wagner F. 2007 *Plasma Phys. Control. Fusion* **49** B1
[3] Itoh K., Itoh S.-I. and Fukuyama A. 1999 *Transport and Structural Formation in Plasmas* (Bristol: Institute of Physics Publishing)
[4] Casper T., Gribov Y., Kavin A., Lukash V., Khayrutdinov R., Fujieda H., Kessel C. and ITER Domestic Agencies 2013 *Nucl. Fusion* **54** 013005
[5] Wagner F. *et al* 1982 *Phys. Rev. Lett.* **49** 1408
[6] Itoh S.-I. and Itoh K. 1988 *Phys. Rev. Lett.* **60** 2276
[7] Shaing K.C. and Crume Jr E.C. 1989 *Phys. Rev. Lett.* **63** 2369
[8] Groebner R.J., Burrell K.H. and Seraydarian R.P. 1990 *Phys. Rev. Lett.* **64** 3015
[9] Ida K., Hidekuma S., Miura Y., Fujita T., Mori M., Hoshino K., Suzuki N., Yamauchi T. and JFT-2M group 1990 *Phys. Rev. Lett.* **65** 1364
[10] ASDEX Team 1989 *Nucl. Fusion* **29** 1959
[11] Doyle E.J. *et al* 1991 *Phys. Fluids B* **3** 2300
[12] Matsumoto H. *et al* 1992 *Plasma Phys. Control. Fusion* **34** 615
[13] Tynan G.R., Schmitz L., Conn R.W., Doerner R. and Lehmer R. 1992 *Phys. Rev. Lett.* **68** 3032
[14] Cordey J.G. *et al* 1995 *Nucl. Fusion* **35** 505
[15] Ido T., Kamiya K., Miura Y., Hamada Y., Nishizawa A. and Kawasumi Y. 2002 *Phys. Rev. Lett.* **88** 055006
[16] Burrell K.H. 1997 *Phys. Plasmas* **4** 1499
[17] Biglari H., Diamond P.H. and Terry P.W. 1990 *Phys. Fluids* B **2** 1
[18] Itoh S.-I. and Itoh K. 1990 *J. Phys. Soc. Jpn* **59** 3815
[19] Terry P.W. 2000 *Rev. Mod. Phys.* **72** 109
[20] Tynan G.R., Cziegler I., Diamond P.H., Malkov M., Hubbard A., Hughes J.W., Terry J.L. and Irby J.H. 2016 *Plasma Phys. Control. Fusion* **58** 044003
[21] Itoh K. and Itoh S.-I. 1996 *Plasma Phys. Control. Fusion* **38** 1
[22] Stringer T.E. 1993 *Nucl. Fusion* **33** 1249
[23] Diamond P.H., Itoh S.-I., Itoh K. and Hahm T.S. 2005 *Plasma Phys. Control. Fusion* **47** R35
[24] Fujisawa A. *et al* 2004 *Phys. Rev. Lett.* **93** 165002
[25] Gupta D.K., Fonck R.J., McKee G.R., Schlossberg D.J. and Shafer M.W. 2006 *Phys. Rev. Lett.* **97** 125002
[26] Liu A.D. *et al* 2009 *Phys. Rev. Lett.* **103** 095002
[27] Hillesheim J.C., Delabie E., Meyer H., Maggi C.F., Meneses L., Poli E. and JET Contributors 2016 *Phys. Rev. Lett.* **116** 065002
[28] Kim E.J. and Diamond P.H. 2003 *Phys. Rev. Lett.* **90** 185006
[29] Kobayashi T. *et al* 2016 *Sci. Rep.* **6** 30720
[30] Shaing K.-C., Hazeltine R.D. and Sanuki H. 1992 *Phys. Fluids* B **4** 404
[31] Hassam A.B. and Drake J.F. 1993 *Phys. Fluids B* **5** 4022
[32] Rosenbluth M.N. and Hinton F.L. 1996 *Nucl. Fusion* **36** 55
[33] Rosenbluth M.N. and Hinton F.L. 1998 *Phys. Rev. Lett.* **80** 724
[34] Askinazi L.G., Golant V.E., Kornev V.A., Lebedev S.V., Tukachinsky A.S., Vildjunas M.I. and Zhubr N.A. 2006 *Plasma Phys. Control. Fusion* **48** A85
[35] Bulanin V.V., Askinazi L.G., Lebedev S.V., Gorohov M.V., Kornev V.A., Petrov A.V., Tukachinsky A.S. and Vildjunas M.I. 2006 *Plasma Phys. Control. Fusion* **48** A101
[36] Taylor R.J., Brown M.L., Fried B.D., Grote H., Liberati J.R., Morales G.J., Pribyl P., Darrow D. and Ono M. 1989 *Phys. Rev. Lett.* **63** 2365
[37] Weynants R.R. *et al* 1992 *Nucl. Fusion* **32** 837
[38] Askinazi L.G., Golant V.E., Lebedev S.V., Rozhanskij V.A. and Tendler M. 1992 *Nucl. Fusion* **32** 271
[39] Kirnev G.S. *et al* 2003 *Plasma Phys. Control. Fusion* **45** 337
[40] Rozhansky V., Kaveeva E., Voskoboynikov S., Coster D., Bonnin X. and Schneider R. 2002 *Phys. Plasmas* **9** 3385–94
[41] Itoh K., Itoh S.-I., Kamiya K. and Kasuya N. 2015 *Plasma Phys. Control. Fusion* **57** 075008
[42] Staebler G.M., Hinton F.L., Wiley J.C., Dominguez R.R., Greenfield C.M., Gohil P., Kurki-Suonio T.K. and Osborne T.H. 1994 *Phys. Plasmas* **1** 909–26
[43] Moyer R.A. *et al* 1995 *Phys. Plasmas* **2** 2397
[44] Kamiya K. *et al* 2010 *Phys. Rev. Lett.* **105** 045004
[45] Viezzer E., Pütterich T., Angioni C., Bergmann A., Dux R., Fable E., McDermott R.M., Stroth U., Wolfrum E. and the ASDEX Upgrade team 2013 *Nucl. Fusion* **54** 012003
[46] Hinton F.L. and Hazeltine R.D. 1976 *Rev. Mod. Phys.* **48** 239
[47] Peeters A.G. 2000 *Phys. Plasmas* **7** 268
[48] Sauter P. *et al* 2011 *Nucl. Fusion* **52** 012001
[49] Ryter F. *et al* 2013 *Nucl. Fusion* **53** 113003
[50] Yan Z., Gohil P., McKee G.R., Eldon D., Grierson B., Rhodes T. and Petty C.C. 2017 *Nucl. Fusion* **57** 126015
[51] Viezzer E. *et al* 2016 *Nucl. Fusion* **57** 022020
[52] Kobayashi T. *et al* 2017 *Nucl. Fusion* **57** 072005
[53] Kobayashi T. *et al* 2015 *Nucl. Fusion* **55** 063009
[54] Ido T., Hamada Y., Nishizawa A., Kawasumi Y., Miura Y. and Kamiya K. 1999 *Rev. Sci. Instrum.* **70** 955
[55] Ido T., Kamiya K., Hamada Y., Nishizawa A., Kawasumi Y. and Miura Y. 1999 *Plasma Phys. Control. Fusion* **41** 1013
[56] Fujisawa A. *et al* 1997 *Phys. Rev. Lett.* **79** 1054
[57] Estrada T., Happel T., Hidalgo C., Ascasibar E. and Blanco E. 2010 *Europhys. Lett.* **92** 35001
[58] Conway G.D., Angioni C., Ryter F., Sauter P., Vicente J. and ASDEX Upgrade Team 2011 *Phys. Rev. Lett.* **106** 065001
[59] Xu G.S. *et al* 2011 *Phys. Rev. Lett.* **107** 125001
[60] Schmitz L., Zeng L., Rhodes T.L., Hillesheim J.C., Doyle E.J., Groebner R.J., Peebles W.A., Burrell K.H. and Wang G. 2012 *Phys. Rev. Lett.* **108** 155002
[61] Cheng J. *et al* 2013 *Phys. Rev. Lett.* **110** 265002
[62] Kobayashi T. *et al* 2013 *Phys. Rev. Lett.* **111** 035002
[63] Kobayashi T. *et al* 2014 *Nucl. Fusion* **54** 073017
[64] Cavedon M. *et al* 2016 *Nucl. Fusion* **57** 014002
[65] Birkenmeier G. *et al* 2016 *Nucl. Fusion* **56** 086009
[66] Solano E.R. *et al* 2016 *Nucl. Fusion* **57** 022021
[67] Yashin A.Y., Bulanin V.V., Gusev V.K., Kurskiev G.S., Patrov M.I., Petrov A.V., Petrov Y.V. and Y. Tolstyakov S. 2018 *Nucl. Fusion* **58** 112009
[68] Grover O. *et al* 2018 *Nucl. Fusion* **58** 112010
[69] Liang A.S. *et al* 2018 *Phys. Plasmas* **25** 022501
[70] Shao L.M. *et al* 2018 *Plasma Phys. Control. Fusion* **60** 035012
[71] Manz P. *et al* 2012 *Phys. Plasmas* **19** 072311
[72] Shesterikov I. *et al* 2013 *Phys. Rev. Lett.* 111 055006
[73] Yan Z., McKee G.R., Fonck R., Gohil P., Groebner R.J. and Osborne T.H. 2014 *Phys. Rev. Lett.* **112** 125002
[74] Park G.Y., Kim S.S., Jhang H., Diamond P.H., Rhee T. and Xu X.Q. 2015 *Phys. Plasmas* **22** 032505
[75] Yan Z. *et al* 2019 Role of turbulence mode velocity shear in triggering the L–H transition across multiple parameters *17th Int. Workshop on H-Mode Physics and Transport Barriers* (Shanghai, China)
[76] Chang C.S., Ku S., Tynan G.R., Hager R., Churchill R.M., Cziegler I., Greenwald M., Hubbard A.E. and Hughes J.W. 2017 *Phys. Rev. Lett.* **118** 175001
[77] Ku S. *et al* 2018 *Phys. Plasmas* **25** 056107
[78] Chôné L., Beyer P., Sarazin Y., Fuhr G., Bourdelle C. and Benkadda S. 2015 *Nucl. Fusion* **55** 073010
[79] Diallo A., Banerjee S., Zweben S.J. and Stoltzfus-Dueck T. 2017 *Nucl. Fusion* **57** 066050
[80] Manz P. *et al* 2016 *Phys. Plasmas* **23** 052302
[81] Cheng J., Xu Y., Yan L.W., Xu J.Q., Huang Z.H., Wu N., Shi Z.B., Liu Y, and Xu M. 2019 Experimental

observation of nonlinear coupling of electromagnetic modes leading to the onset of H mode in toroidal plasmas *17th Int. Workshop on H-Mode Physics and Transport Barriers* (Shanghai, China)
[82] Itoh K., Itoh S.-I. and Fujisawa A. 2013 *Plasma Fusion Res.* **8** 1102168
[83] Pütterich T., Wolfrum E., Dux R., Maggi C.F. and ASDEX Upgrade Team 2009 *Phys. Rev. Lett.* **102** 025001
[84] Ido T. *et al* 2006 *Nucl. Fusion* **46** 512
[85] Ido T. *et al* 2006 *Plasma Phys. Control. Fusion* **48** S41
[86] Kobayashi T. *et al* 2018 *Phys. Rev. Lett.* **120** 045002
[87] Itoh K., Hallatschek K. and Itoh S.-I. 2005 *Plasma Phys. Control. Fusion* **47** 451
[88] Honda M. and Fukuyama A. 2016 *Comput. Phys. Commun.* **208** 117
[89] Kim E.J. and Diamond P.H. 2003 *Phys. Rev. Lett.* **91** 075001
[90] Carreras B.A., Lynch V.E. and Garcia L. 1991 *Phys. Fluids* B **3** 1438
[91] Powers E.J. 1974 *Nucl. Fusion* **14** 749
[92] Boedo J.A., Gray D.S., Terry P.W., Jachmich S., Tynan G.R., Conn R.W. and TEXTOR-94 Team 2002 *Nucl. Fusion* **42** 117
[93] Shats M.G. *et al* 2000 *Phys. Rev. Lett.* **84** 6042
[94] Antoni V., Martines E., Desideri D., Fattorini L., Serianni G., Spolaore M., Tramontin L. and Vianello N. 2000 *Plasma Phys. Control. Fusion* **42** 83
[95] Terry P.W., Newman D.E. and Ware A.S. 2001 *Phys. Rev. Lett.* **87** 185001
[96] Schaffner D.A., Carter T.A., Rossi G.D., Guice D.S., Maggs J.E., Vincena S. and Friedman B. 2012 *Phys. Rev. Lett.* **109** 135002
[97] Schaffner D.A., Carter T.A., Rossi G.D., Guice D.S., Maggs J.E., Vincena S. and Friedman B. 2013 *Phys. Plasmas* **20** 055907
[98] Itoh K., Itoh S.-I., Kamiya K. and Kobayashi T. 2017 *Nucl. Fusion* **57** 022005
[99] Kamiya K., Itoh K. and Itoh S.-I. 2016 *Sci. Rep.* **6** 30585
[100] Zarzoso D. *et al* 2013 *Phys. Rev. Lett.* **110** 125002
[101] Sasaki M., Itoh K., Hallatschek K., Kasuya N., Lesur M., Kosuga Y. and Itoh S.-I. 2017 *Sci. Rep.* **7** 16767
[102] Sasaki M., Kobayashi T., Itoh K., Kasuya N., Kosuga Y., Fujisawa A. and Itoh S.-I. 2018 *Phys. Plasmas* **25** 012316
[103] Birkenmeier G., Ramisch M., Schmid B. and Stroth U. 2013 *Phys. Rev. Lett.* **110** 145004
[104] Kobayashi T. 2017 *Sci. Rep.* **7** 14971
[105] Hahm T.S., Diamond P.H., Lin Z., Itoh K. and Itoh S.-I. 2004 *Plasma Phys. Control. Fusion* **46** A323
[106] Gürcan Ö.D., Diamond P.H., Hahm T.S. and Lin Z. 2005 *Phys. Plasmas* **12** 032303
[107] Garbet X., Sarazin Y., Imbeaux F., Ghendrih P., Bourdelle C., Gürcan Ö.D. and Diamond P.H. 2007 *Phys. Plasmas* **14** 122305
[108] Estrada T., Hidalgo C. and Happel T. 2011 *Nucl. Fusion* **51** 032001
[109] Grenfell G. *et al* 2019 *Nucl. Fusion* **59** 016018
[110] Leconte M. and Singh R. 2019 *Plasma Phys. Control. Fusion* **61** 095004
[111] Baver D.A., Terry P.W., Gatto R. and Fernandez E. 2002 *Phys. Plasmas* **9** 3318
[112] Kaw P., Singh R. and Diamond P.H. 2001 *Plasma Phys. Control. Fusion* **44** 51
[113] Tokuzawa T. *et al* 2014 *Phys. Plasmas* **21** 055904
[114] Kim C.-B., Min B. and An C.-Y. 2019 *Plasma Phys. Control. Fusion* **61** 035002
[115] Hasegawa A. and Wakatani M. 1983 *Phys. Rev. Lett.* **50** 682
[116] Jenko F. and Scott B.D. 1999 *Phys. Plasmas* **6** 2705
[117] Bonanomi N., Angioni C., Crandall P.C., Di Siena A., Maggi C.F., Schneider P.A., the ASDEX Upgrade Team, the EUROFusion MST1 Team and JET Contributors 2019 *Nucl. Fusion* **59** 126025
[118] De Dominici G., Fuhr G., Bourdelle C., Beyer P., Garbet X., Sarazin Y., Falchetto G.L. and JET Contributors 2019 *Nucl. Fusion* **59** 126019
[119] Kaang H.H., Jhang H., Singh R., Kim J. and Kim S.S. 2016 *Phys. Plasmas* **23** 052501
[120] Sasaki M., Itoh K., Kosuga Y., Dong J.Q., Inagaki S., Kobayashi T., Cheng J., Zhao K.J. and Itoh S.-I. 2019 *Nucl. Fusion* **59** 066039
[121] Kong D.F. *et al* 2018 *Nucl. Fusion* **58** 034003
[122] Kosuga Y., Itoh S.-I. and Itoh K. 2015 *Plasma Fusion Res.* **10** 3401024
[123] Inagaki S. *et al* 2016 *Sci. Rep.* **6** 22189
[124] Kobayashi T. *et al* 2016 *Phys. Plasmas* **23** 102311